Modeling Quantum Dots in Realistic Carbon Nanotube Devices

thesis for the degree
Master of Science
Thomas Balder

February 2008

Delft University of Technology
Faculty of Applied Sciences
Kavli Institute of Nanoscience
Quantum Transport Group
Dr. Gary Steele
Prof. dr. ir. Leo P. Kouwenhoven

Abstract

In this work, simulation results on realistic carbon nanotube devices are presented. A simulation program was developed to model quantum dots in semiconducting nanotubes, being controlled by external gates only. The simulation program numerically solves the Poisson equation, and can be combined with the Thomas-Fermi approximation and Hartree approximation to model the many electron regime for the nanotube. For two electrons in a double quantum dot, exact solutions of the two-electron Schrödinger equation are presented, where screening of the gates and leads in the modeled device is included in the external potential, as well as in the Coulomb interaction between the two electrons.

Classical 3D electrostatic simulations have shown that suspending a nanotube results in a better coupling of the quantum dot to the single electron transistor (SET) and that back-action is reduced. Overall sensitivity of the SET is increased by suspending the nanotube.

We have used the Thomas-Fermi approximation to show that splitgates can be used to control a quantum dot in a semiconducting nanotube. The Hartree approximation is used to calculate the addition energy for different number of electrons in a single quantum dot. For a quantum dot with about 40 electrons, the charging energy is $E_C \approx 20\,\mathrm{meV}$ and the level spacing equals $\delta = 0.8\,\mathrm{meV}$. The self-consistent spectrum obtained from the Hartree approximation is different from the spectrum corresponding to the Thomas-Fermi approximation. The spectrum, addition energy, and level spacing are (strongly) dependent on the number of electrons in the dot.

Results from exact diagonalization of the two-electron Schrödinger equation show that the singlet-triplet splitting in a single dot is much lower than expected. We use the harmonic oscillator model to qualitatively show that the electrons, in a realistic potential for a nanotube, will separate to save Coulomb energy, such that the shell filling model no longer applies. The separation of the electrons is similar to the formation of a Wigner crystal.

Finally, we show that a device with five splitgates can be used to control a double dot. The interdot coupling can be tuned such that it is much smaller than the singlet-triplet splitting, even for the small singlet-triplet splitting observed. Experimentally, the transition from the (1,1) state to the (0,2) state for the calculated gate voltages should occur in a time longer than $\sim 0.7\,\mu\mathrm{s}$. The temperature limit corresponding to the simulation results equals $\sim 25\,\mathrm{mK}$.

Acknowledgments

First of all I would like to thank my supervisor Gary Steele. Since day one he has always been very enthusiastic and encouraging. He always made time free to explain physics and made the complex research done at QT tangible for me. Doing a theoretical project at an experimental group is by itself quite an experiment, but even in this area Gary always had an answer to my questions. His clear explanations, enthusiasm, and great knowledge have been an important factor for the outcome of this project.

My gratitude also goes to Leo Kouwenhoven for making it possible to do a master project at QT. Especially many thanks for making it possible to visit Harvard, where QT is known as *the gang of Leo*. Together with Rob Westervelt from NSEC, he realized this great opportunity for me.

Many thanks go to Michael Stopa, who really made me feel like home at Harvard. In the short time I have been there, we had many very fruitful discussions which resulted in some nice improvements for the project. It was great to work with him and learn the ins and outs of the dark art of numerical modeling of realistic devices.

Other people I would like to thank are Björn Trauzettel for the detailed explanations by email, Jos Thijssen for the suggestion to use an exact solution for the two-electron problem, Naomi Brave for arranging my actual stay at Harvard, and all people from QT who helped me in the past year.

Finally, I would like to thank my family and friends for the support they gave me in the sometimes stressful period, and especially my girlfriend Sietske Vellema, who was always there for me.

Contents

Chapter 1

Introduction

1.1 The quantum computer

In 1947, the American computer engineer Howard Aiken said that just six electronic digital computers would satisfy the computing needs of the United States. Of course, at this time it was not know that scientific research, personal computers and the internet would fuel the thirst for more and more computational power. According to Moore's law, the scale of the computer chips decreases by a factor two every 18 months, which would mean that in ten to twenty years, the transistors on a microchip would be of the order of nanometers. From this point of view it is unavoidable that at some point, a new type of computer will be introduced, called the quantum computer.

A quantum computer is fundamentally different from the classical computer. A classical computer stores information in a bit, which can have the value of either 0 or 1. In a quantum computer, the information is stored in a two-level quantum system, called quantum bit, or qubit. The large difference between the classical bit and the qubit is that the qubit uses the quantum nature to represent data. This means that the qubit can have the value of 0 and 1 at the same time, as well as any value in between. In other words, the qubit is in a superposition of 0 and 1.

Quantum computations are done by manipulating this qubit. When two or more qubits are coherently connected to each other, they together form one coherent quantum state. An operation on one qubit is then actually an operation on all the qubits at the same time. This results in an exponentially increase of computational power for a linear increase of the number of qubits. Using this property, certain algorithms can be performed exponentially faster than any conventional computer will ever can. One of such algorithms is Shor's algorithm, used to factorize prime numbers for cryptographical applications. Factorizing large prime numbers on a classical computer requires a exponential time algorithm, while the algorithm used by a quantum computer is polynomial one [1].

1.2 Spin Qubits

Any two level quantum system can in principle be used as a qubit. A few examples are: the ground state and excited state of an atom, the spin up and down of an electron, or the horizontal and vertical polarization of a photon. However, for the physical implementation of quantum computation, the requirements defined by DiVincenzo must be met [2]:

- A scalable physical system with well characterized qubits
- The ability to initialize the state of the qubits to a simple fiducial state, such as $|000...\rangle$
- Long relevant decoherence times, much longer than the gate operation time
- A "universal" set of quantum gates
- A qubit-specific measurement capability

One of the most promising qubits is the spin of the electron, confined in a quantum dot [3]. The main problem of nanoscale devices is the electric noise causing decoherence of qubits. Spin qubits however, are not effected by electric noise and are therefore good candidates for future quantum computers.

For many years, devices have been fabricated where one or more electrons are confined in all three dimensions by an electrostatic confinement potential in a GaAs two dimensional electron gas (2DEG). The electrons are confined in a so called quantum dot, which can be compared with an artificial atom, where the electron states are well defined. The number of electrons as well as the states of single electrons can be controlled using external gates and a magnetic field. It has been shown that, in this way, all needed quantum operations can be performed on the spin qubit, such as the control of exchange interaction between two electrons and rotation of a the spin of a single electron [4, 5].

However, one of the requirements of DiVincenzo is "long relevant decoherence times, much longer than the gate operation". In GaAs devices, the net spin of about 10^6 nuclei couples to the spin of the electrons in the quantum dot, significantly decreasing the coherence time of the qubit. [6, 7]. Also, the heavy Ga and As atoms result in strong spin orbit coupling, causing the spins of the electrons to flip through non-magnetic interactions, such as phonons. Finally, hyperfine interaction causes an effective non-uniform magnetic field in the sample and therefore incoherent manipulation of the qubits, reducing the spin coherence time.

1.3 Carbon nanotubes

One solution to the problems of GaAs devices is using the spin of an electron in a quantum dot in a carbon nanotube as a qubit. Carbon nanotubes were discovered by S. Iijima, in 1991 [8]. A carbon nanotube is a cylinder of carbon atoms with a diameter of typically 1 nm, and a length of typically thousands times longer. Nanotubes are exceptionally strong and have unique electrical properties. For example, the alignment of the carbon atoms forming the cylinder determines whether a nanotube is metallic of semiconducting.

Apart from interesting physics, using carbon nanotubes has other advantages. First of all, carbon atoms C^{12} have zero nuclear spin. Second, hyperfine interaction is small since carbon is a light atom. Moreover, the electronic states of a nanotube are defined by *p*-orbitals, for which the contact term of the hyperfine interaction vanishes. The light carbon atoms also reduces the spin-orbit coupling pre-factor with almost two orders of magnitude, compared to GaAs systems. Finally, fabricating nanotube devices can be done in a very clean way. For regular growth techniques, a typical carbon nanotube consist for only 1.1% of C^{13} atoms, making it a very clean system suitable for creating quantum dots and spin qubits. Because of these arguments, the coherence time for a spin qubit in a nanotube is expected to be long [9].

All together, a carbon nanotube is a remarkably interesting and useful system, having great potential in being the replacement of conventional semiconductor microelectronics.

1.4 Motivation

Although much work has already been realized in the research field of carbon nanotubes [10–20], there is yet much to be explored. Many features of future objectives are hard to predict. The main reason for this is that nanoscale systems involve multi-scale physics. Therefore, nanoscale systems can be very complex, and are almost always too complex to be described with analytical equations. Numerical simulations are the solution to modeling realistic (carbon nanotube) devices, giving a better insight in, and understanding of, experimental results. This is the main motivation for the work presented in this thesis.

A second motivation for the development of a simulation program for realistic devices is to use it to support the design of new devices. Fabrication of nanodevices usually requires a good recipe and much experience, but even then, fabricating the desired device takes many attempts and thus a lot of time. Using the simulation program, full 3D self-consistent electrostatics for different gate geometries can be easily calculated, and this can be combined with the 1D quantum mechanical processes at the nanotube. This makes numerical simulations very useful to optimize the fabrication process by testing new gate geometries without having to actually fabricate them.

Chapter 2

Background theory on nanotubes and quantum dots

The final goal of this master project is to calculate the electronic states in a double quantum dot in realistic carbon nanotube devices. This chapter discusses the relevant theoretical background which is needed to do these calculations. First the electronic properties of nanotubes are discussed. Then, the quantum dot, the double dot and the double dot experiment are explained. Finally, the many body Hamiltonian is introduced.

Since this thesis is about a theoretical work, a chapter about fabrication of nanodevices will be absent. However, we will briefly discuss some designs of devices which could be used to make quantum dots in semiconducting nanotubes in subsection 2.2.2.

2.1 From 2D graphene to a 1D nanotube

A carbon nanotube is a small cylinder of the order of 1 nm, which can be thought of as a rolled up sheet of graphene. Graphene, the 2D equivalent of graphite, consists of a single layer of carbon atoms, ordered in a hexagonal lattice. The ground state of one carbon atom is given by $1s^2 2s^2 2p_x^1 2p_y^1 2p_z^0$. In the hexagonal lattice, the $2s^2$ electrons mix with two of the p-orbitals such that three in-plane sp^2 σ-bonds with a 120° angle are formed. The remaining p_z-orbital, perpendicular to the graphene sheet, forms delocalized π-bonds and π^*-antibonds due to interactions with the neighboring p_z-orbitals of other carbon-atoms. In contrast to the energy levels of the π-electrons, the energy levels of the σ-bonds are far away from the Fermi energy. Therefore, the π-electrons are mainly responsible for the transport properties of graphene [21, 22].

One of the most interesting aspects about nanotubes is that its electronic properties are determined by way the graphene sheet is rolled up. The way the sheet is rolled can be described by a chiral vector:

$$\vec{C} = n_1 \vec{a_1} + n_2 \vec{a_2} \equiv (n_1, n_2) \tag{2.1}$$

with integers n_1 and n_2, and vectors $\vec{a_1}$ and $\vec{a_2}$ defined by

$$\vec{a_1} = \left(\frac{\sqrt{3}}{2}; \frac{1}{2} \right) a_0 \quad \text{and} \quad \vec{a_2} = \left(\frac{\sqrt{3}}{2}; -\frac{1}{2} \right) a_0 \tag{2.2}$$

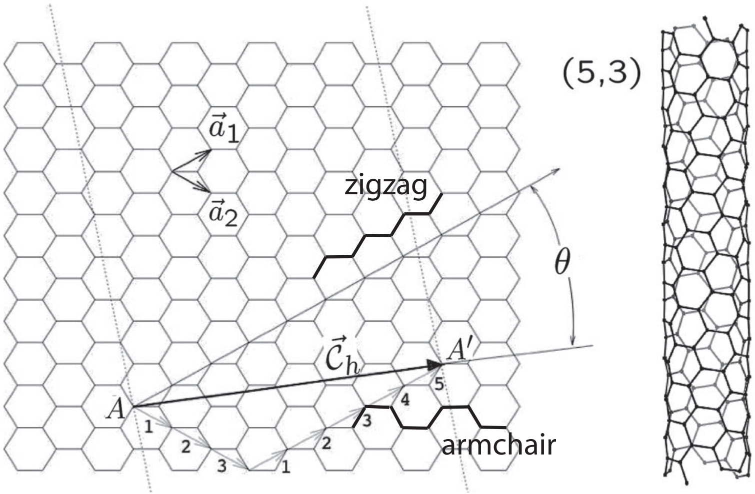

Figure 2.1: Graphene lattice with vectors $\vec{a_1}$ and $\vec{a_2}$. In the example drawn corresponds to a $(5,3)$ nanotube as given on the right. Figure is adapted from [21].

with $a_0 = \sqrt{3}a_{CC} = 2.46\,\text{Å}$. Every nanotube can be uniquely described by this chiral vector. From the chiral vector the diameter follows via

$$d = \frac{|\vec{C}|}{\pi} = \frac{a_0}{\pi}\sqrt{n_1^2 + n_2^2 + n_1 n_2} \tag{2.3}$$

and the angle between $\vec{C}$ and $\vec{a_1}$, the chiral angle θ, is given by

$$\theta = \arccos\left(\frac{\vec{C}\cdot\vec{a_1}}{|\vec{C}||\vec{a_1}|}\right) = \arccos\left(\frac{2n_1 + n_2}{2\sqrt{n_1^2 + n_2^2 + n_1 n_2}}\right) \tag{2.4}$$

as illustrated in Fig. 2.1.

Because of the hexagonal symmetry of the honeycomb lattice, the chiral angle is $0 \leq |\theta| \leq 30\,°$. The example given in Fig. 2.1 corresponds to a $(5,3)$ nanotube with a diameter of 1.72 nm and chiral angle $\theta = 21.8\,°$. Two special cases exist: nanotubes with chiral angle $\theta = 0\,°$, (n_1, n_1) nanotubes, are called armchair tubes, and $(n_1, 0)$ nanotubes are of the type zigzag, with chiral angle $\theta = 30\,°$. Both cases are achiral tubes.

The translational vector $\vec{T}$, perpendicular to $\vec{C}$, reads

$$\vec{T} = \frac{2n_2 + n_1}{N_R}\vec{a_1} - \frac{2n_1 + n_2}{N_R}\vec{a_2} \tag{2.5}$$

where N_R is the greatest common divisor of the two numerators $2n_2 + n_1$ and $2n_1 + n_2$. The vectors $\vec{C}$ and $\vec{T}$ describe the primitive cell of a (n_1, n_2) nanotube, from which a nanotube can be constructed: a cylinder of height $|\vec{T}|$ and circumference $|\vec{C}|$. The electronic properties depend strongly on the primitive cell. The $(5,3)$ nanotube is, for example, a semi-conducting nanotube, while a $(6,3)$ nanotube is metallic. In general, because of the symmetry, a nanotube is metallic if $n_1 - n_2$ is a multiple of 3. In the next section we will discuss this in more detail.

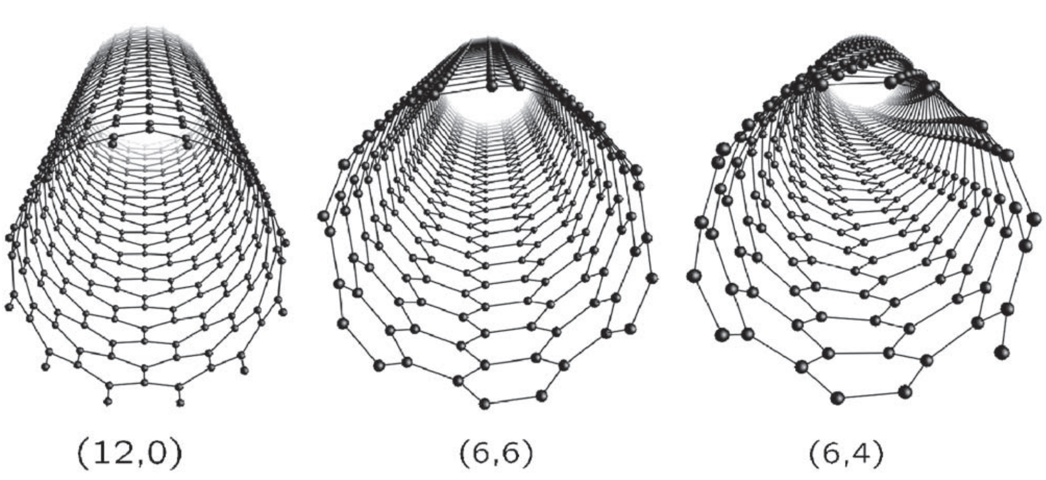

Figure 2.2: Three types of nanotubes, zigzag (left), armchair (middle) and chiral (right). Figure is adapted from [21].

2.1.1 Band structure

In Fig. 2.3, the unit cell of graphene is drawn on the hexagonal lattice of carbon atoms. Using the vectors $\vec{a_1}$ and $\vec{a_2}$, all lattice sites can be mapped onto two inequivalent sites, labeled A and B. This means that the unit cell contains only two atoms.

The reciprocal vectors of the unit cell are given by

$$\vec{b_1} = \left(\frac{1}{\sqrt{3}};1\right)\frac{2\pi}{a_0} \quad \text{and} \quad \vec{b_2} = \left(\frac{1}{\sqrt{3}};-1\right)\frac{2\pi}{a_0} \tag{2.6}$$

Using the tight binding model, the 2D-dispersion relation of graphene can be found [23]:

$$E^{\pm}(k_x,k_y) = \pm\gamma_0\sqrt{1+4\cos\frac{\sqrt{3}k_x a_0}{2}\cos\frac{k_y a_0}{2}+4\cos^2\frac{k_y a_0}{2}} \tag{2.7}$$

where γ_0 is the tight binding nearest neighbor overlap energy, $\gamma_0 = 2.9\,\mathrm{eV}$. The vector $\vec{k} = (k_x, k_y)$ is a set of available electronic momenta corresponding to the first Brillouin zone.

The valence and conduction band of graphene, the π-states, touch at the six corners of the hexagonal Brillouin zone, called the K points. Since the conduction and valence band cross at these points (charge neutrality points), the Fermi surface is defined by this set of K points.

From the band structure of graphene, the band structure of a nanotube can be derived. For a 1D nanotube, the wave function around the nanotube must satisfy the boundary condition

$$\Psi(\vec{r}+\vec{C}) = e^{i\vec{k}\cdot\vec{C}}\Psi(\vec{r}) = e^{i2\pi}\Psi(\vec{r}) = \Psi(\vec{r}) \tag{2.8}$$

This boundary condition results in a set of allowed discrete values for k, which can be projected onto the Brillouin zone of graphene (Fig. 2.4). In the direction along the nanotube, the wave vectors are continuous (assuming an infinite long nanotube).

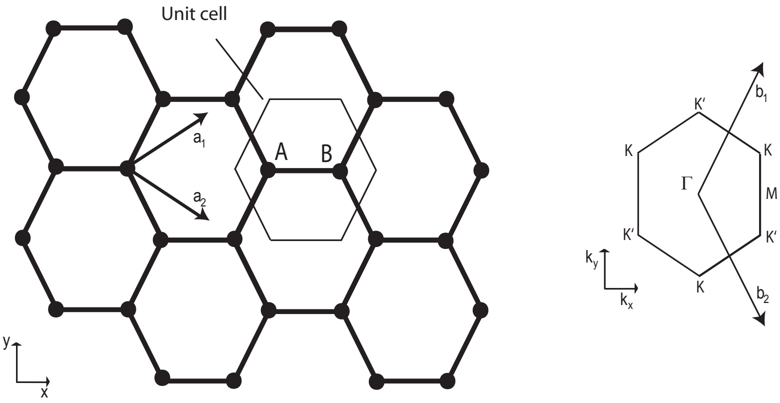

Figure 2.3: Left: The hexagonal lattice of graphene with the basis vectors and unit cell. Right: Brillouin zone with reciprocal basis vectors $\vec{b1}$ and $\vec{b_2}$ and Γ, K,K' and M points (symmetry directions).

From Eq.(2.8) the discrete set of allowed k-vectors follows:

$$k(n) = \frac{2\pi}{|\vec{C}|}\left(n - \frac{n_1 - n_2 - 3N}{3}\right) \quad n = 0, \pm 1, \pm 2, ... \quad N = 0, 1, 2, ... \tag{2.9}$$

Here, n is the subband index and N is an integer, such that

$$k(n) = \frac{2\pi}{|\vec{C}|}\left(n - \frac{\nu}{3}\right) \quad n = 0, \pm 1, \pm 2, ... \quad \nu = 0, \pm 1 \tag{2.10}$$

with ν defined by $\nu = n_1 - n_2 - 3N$.

In zero magnetic field, the k-vector intersects the Brillouin zone at a K-point, for $\nu = 0$. For $\nu = \pm 1$, the closest k-vector to the K-points has an offset of $\Delta k = \pm 2\pi/3|\vec{C}| = \pm 2/3d$.

The 1D dispersion relation for a nanotube is obtained by slicing the 2D dispersion relation relation of graphene (Eq.(2.7)) at the given set of k-vectors, yielding [21]:

$$E_{\pm n}(k_{\|}) = \pm \beta \sqrt{k(n)^2 + k_{\|}^2} \tag{2.11}$$

with $\beta = \sqrt{3} a_0 \gamma_0 / 2$. Each energy band is two-fold degenerate in zero magnetic field, except for the case where $n = 0$ and $\nu = 0$. The degeneracy is called $K\,K'$ degeneracy, or valley degeneracy, with K and K' corresponding to a different valley. Each two-fold degenerate energy band is again two-fold spin degenerate, resulting in four-fold degenerate energy bands.

The lowest conduction band and the highest valence band are given by $+\beta|k(0)|$ and $-\beta|k(0)|$ respectively. For $\nu = 0$ ($n_1 + n_2$ is a multiple of 3) it follows that $+\beta|k(0)| = -\beta|k(0)|$. For these cases, the dispersion relation is linearly proportional to $k_{\|}$ and crosses at the K-point. This means that there is no gap at $E = E_F$, and thus the nanotube is metallic.

For semiconducting nanotubes, with $\nu = \pm 1$, there is no integer n for which $k(n) = 0$ holds, so a gap opens at the Fermi level. Assuming a linear dispersion relation near the Fermi energy, the energy of the gap is

$$E_g(k_{\|} = 0) = 2\beta|k(0)| = 2\frac{\sqrt{3} a_0 \gamma_0}{2} \cdot \frac{2}{d} \cdot \frac{1}{3} = \frac{2 a_0 \gamma_0}{\sqrt{3} d} \tag{2.12}$$

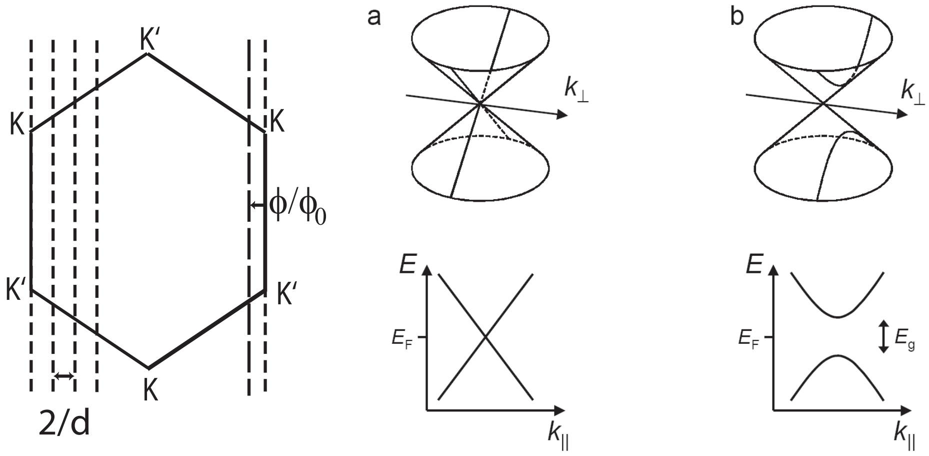

Figure 2.4: Left: First Brillouin zone of graphene with the allowed states of a armchair nanotube projected. A magnetic flux ϕ/ϕ_0 parallel to the nanotube axis can be used to shift the allowed states. Figure is adapted from [21].
Right: Energy diagram of the lowest subbands. a) for $\nu = 0$, the k-vector crosses at the K-point, so the subbands cross at $E = E_F$, corresponding to a metallic nanotube. b) for $\nu = \pm 1$, a gap opens and the nanotube is semiconducting. Figure is adapted from [24].

The bandgap is independent of the chiral angle and is inversely proportional to the diameter of the nanotube. However, for small nanotubes, electronic states close to the Fermi level are strongly influenced by other effects such as strain, and atomic defects, which can shift the k-vectors and thus break the $K\,K'$ degeneracy [25]. For larger tubes, the electronic states are determined by the states near the K and K'-points and further effects can in principle be neglected [22]. In this thesis, we will restrict ourselves to metallic nanotubes, and semiconducting nanotubes of which the bandgap can be described with Eq.(2.12).

Apart from atomic defects, strain, and other (undesired) phenomena, the $K\,K'$ degeneracy can also be broken with a small magnetic field parallel to the nanotube (see Fig. 2.4). Including the magnetic field, Eq.(2.9) becomes

$$k(n) = \frac{2\pi}{|\vec{C}|}\left(n - \frac{\nu}{3} + \frac{\phi}{\phi_0}\right) \qquad n = 0, \pm1, \pm2, ... \quad \nu = 0, \pm 1 \tag{2.13}$$

where ϕ_0 is the flux quantum $\phi_0 = ch/|e|$. The coupling of the magnetic field to the valleys is an order of magnitude larger compared to the coupling to the spin of the electrons [20]. Therefore, in our calculations, we will assume that the $K\,K'$ energies can be split, using a very small parallel magnetic field.

2.1.2 Density of States

The electronic states of the nanotubes treated in this thesis are assumed to be defined by the states near the K points and to be insensitive to atomic defects. For this assumption we can use the effective mass approximation. Rewriting Eq.(2.11) and Eq.(2.12)results in an equation for the effective mass m^*:

$$E_{\pm n}(k_{||}) = \pm\sqrt{(m^* v_F^2)^2 + (\hbar k_{|} \| v_F)^2} \tag{2.14}$$

$$m^* = \frac{E_g}{2v_F^2} = \frac{\sqrt{3}a_0\gamma_0}{2dv_F} \tag{2.15}$$

where v_F is the Fermi velocity,

$$v_F = \frac{\sqrt{3}a_0\gamma_0}{2\hbar} \tag{2.16}$$

Using $a_0 = 2.46\,\text{Å}$ and $\gamma_0 = 2.9\text{eV}$, the Fermi velocity equals $v_F = 9.4 \cdot 10^5\,\text{ms}^{-1}$. The effective mass is proportional to the energy gap and thus inverse proportional to the diameter of the nanotube. For the limit $d \to \infty$ (graphene limit), the effective mass goes to zero. The slope of the dispersion relation near the Fermi level is given by

$$\left|\frac{dE}{dk_{||}}\right| = \frac{\sqrt{3}a_0\gamma_0}{2} \frac{k_{||}}{\sqrt{k(n)^2 + k_{||}^2}} = \hbar v_F \frac{\sqrt{E^2 - (E_g/2)^2}}{E} \tag{2.17}$$

Here we only included the highest valence band and the lowest conduction band, $\pm k(0)$. The density of states is given by

$$\frac{dN}{dE} = \left(\frac{L}{2\pi}\right)^d \oint_{FS} \frac{d\vec{S}}{|\nabla_k E|} = 2 \cdot \frac{L}{2\pi} \cdot \frac{4}{|dE/dk|} \tag{2.18}$$

The first factor 2 comes from the spin degeneracy and the factor 4 is a result of the plus and minus k-branches and the two different valleys (K and K') [26]. Using the electron density per unit length $n = N/L$ and inserting Eq.(2.17) into Eq.(2.18) we get the density of states for a nanotube:

$$\frac{dn}{dE} = \hbar v_F \frac{E}{\sqrt{E^2 - (E_g/2)^2}} = \frac{8}{\sqrt{3}\pi a_0\gamma_0} \frac{E}{\sqrt{E^2 - (E_g/2)^2}} \tag{2.19}$$

For metallic nanotubes $E_g = 0$, resulting in a constant density of states.

2.2 Quantum dots

A quantum dot is a man made nanostructure that can confine electrons (or holes) in all spatial degrees of freedom. The size of a quantum dot is small, such that the energy spectrum of the available states in the quantum dot is quantized. Via tunnel barriers, the quantum dot can be coupled to a source and drain from (to) which electrons can tunnel to (from) the dot. Gates can be used to change the energy in the dot through capacitive coupling, or to tune the barriers between the dot and the source and drain. The quantum dot contains a finite number of electrons (or holes), whereof the number can be controlled by external gates and source and drain bias.

To understand a how a quantum dot works, we use the constant interaction (CI) model to explain the electronic properties of a quantum dot. The CI model assumes that the Coulomb

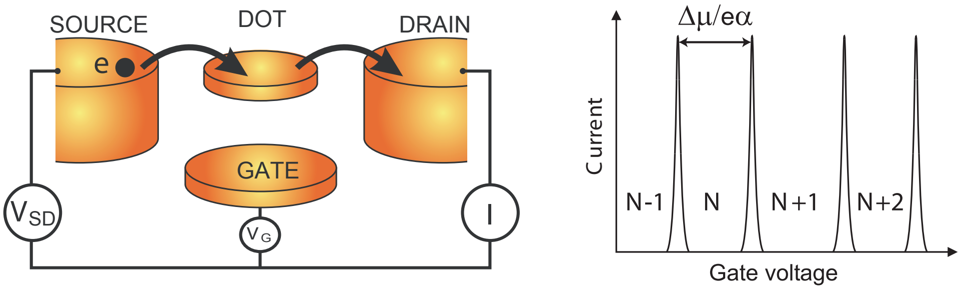

Figure 2.5: Left: Scheme of Quantum dot. The dot is connected to the source and drain via tunnel barriers and coupled capacitively to a gate. The electron tunnel from the source to the dot and from the dot to the drain. The gate is used to electrostatically change the energy of the dot respectively to the source and drain. Figure is adapted from [27]. Right: Current through the dot (I_{SD}) as a function of gate voltage. The number of electrons changes discretely. In between the peaks, there is no current and thus the number of electrons is constant.

interactions of the electrons can be modeled by one quantity: the self capacitance of the dot. The self capacitance C_Σ is defined by the capacitance of the dot to everything else

$$C_\Sigma = C_S + C_D + C_G \tag{2.20}$$

with C_S the capacitance of the dot to the source, C_D the capacitance to the drain and C_G the capacitance to the gate(s).

The second assumption of the model is that the level spacing in the dot is independent of the number of electrons in the dot. Under these two assumptions, the energy of the dot containing N electrons at zero bias ($V_{SD} = 0$) yields

$$U(N) = \frac{(e(N - N_0) + C_G V_G)^2}{2C_\Sigma} + \sum_n E_n \tag{2.21}$$

where N_0 equals the number of electrons in the dot at zero V_G, where V_G is the gate voltage applied. E_n are the single particle energy levels. The energy of the dot is minimal for a particular number of electrons N, depending of the gate voltage applied. The electrochemical potential is defined as the energy of the dot for N electrons minus the energy of the dot for $N - 1$ electrons:

$$\mu_{dot}(N) = U(N) - U(N-1) = \frac{(N - 1/2)e^2 + eC_G V_G}{C_\Sigma} + E_N \tag{2.22}$$

where E_N is energy of the highest filled single electron state. From Eq.(2.22), the addition energy follows:

$$\Delta\mu(N) = \mu(N+1) - \mu(N) = \frac{e^2}{C_\Sigma} + \Delta E \tag{2.23}$$

with ΔE the energy level spacing $E_N - E_{N-1}$[1]. The first term, e^2/C_Σ, is known as the charging energy E_C.

---

[1] For four-fold degenerate orbitals, $\Delta E =$ is only non-zero for every fourth electron

From the CI model, we can conclude that the energy in the dot scales linear with the gate voltage V_G applied. The shift in energy in the dot per voltage applied to the gate is know as the α-factor $\alpha = C_G/C_\Sigma$. When the gate voltage is increased, at some point it becomes energetically more favorable for the system to let an extra electron tunnel into the quantum dot. Consequently, the number of electrons changes discretely as a function of the gate voltage, with period $\Delta\mu/e\alpha$.

Since a quantum dot is small, the self-capacitance, or total capacitance, is also small, and thus the charging energy E_C is large (typically a few meV). To be able to control the number of electrons as described above, there are two requirements that must be met. The first requirement is that temperature is small enough such that the thermal energy is (much) smaller than the charging energy E_C:

$$e^2/C_\Sigma \gg k_B T \tag{2.24}$$

with k_B the Boltzmann constant, $k_B = 1.38 \cdot 10^{-23}\,\mathrm{JK}^{-1} = 86.17\,\mu\mathrm{eVK}^{-1}$.

The second requirement is that the barriers are high enough to localize the electrons, either in the leads, or in the quantum dot. From the Heisenberg uncertainty principle, we can find a lower bound for the resistance of the barriers R_t. Using the discharging time of a capacitor $\Delta t = R_t C_\Sigma$ and $\Delta E = E_C$, we get $(R_t C_\Sigma)(e^2/C_\Sigma) \geq h$, so

$$R_t \gg h/e^2 \tag{2.25}$$

R_t must be (much) larger than the quantum resistance. When these two conditions are met, the electrons are truly confined in the dot and the number of electrons can be changed by the gate(s)[2].

2.2.1 The double dot experiment

The spin of the electron is a good candidate to be used to perform the quantum operations on. In order to be able to use the spin of the electron as a qubit, coherence time of the spin must be sufficiently long. Although interaction with its surrounding is in principle small, it will cause the spin to loose its “memory”. This “memory” time is known as coherence time. Spin coherence time can be measured with a double dot, making use of the spin-blockade, or Pauli-blockade, principle [28].

A double dot consists of two dots separated by a barrier, which is relatively small compared to the barriers between the dots and the environment (leads). Two (or more) independent gates are used to change the chemical potential in each dot separately. When the chemical potentials of both dots are equal, $\mu_L = \mu_R$, the groundstate of two electrons is the singlet $S_{1,1}$ state, where the subindices corresponds to the number of electrons in the left and right dot. Because of the separation of the electrons, the energy difference of the $(1,1)$ singlet and triplet ($S_{1,1}$ and $T_{1,1}$) is very small. In the $S_{0,2}$ and $T_{0,2}$ state, the two electrons are in the same dot. Here, the levelspacing is much larger compared to the (1,1) situation. In the $T_{0,2}$ state, one of the electrons has to occupy a higher orbital, resulting in an energy difference between $T_{0,2}$ and $S_{0,2}$. The experiment is based on the different energies of the singlet-triplet splitting for the (1,1) and (0,2) case.

---

[2] The source and drain can also be used to control the number of electrons. Applying a source-drain bias voltage, a current will flow if $\mu_{Source} > \mu_{dot}(N+1)$ or $\mu_{dot}(N) > \mu_{Drain}$. When $\mu_{Drain} - \mu_{Source} < \Delta\mu(N)$, current is blocked. This is know as Coulomb blockade.

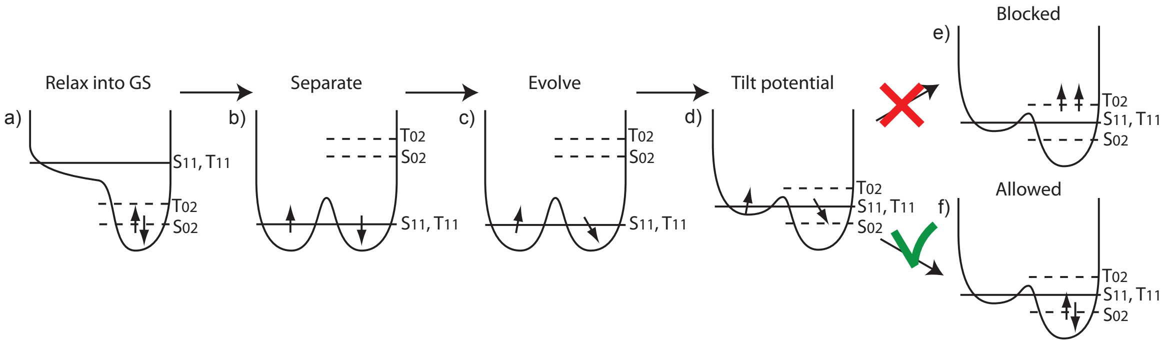

Figure 2.6: The steps of the spin relaxation measurement. First the two electrons are relaxed to their groundstate $S_{0,2}$ (a). Then the chemical potentials of the two dots are aligned and the electrons will separate (b). Because of the delocalization of the electrons, the $S_{1,1}$ and $T_{1,1}$ states are degenerate and can mix due to interactions with the environment (c). If, after some time τ the potential is tilted back again (d), the electrons will occupy the $S_{0,2}$ state when the spins have evolved coherently (f). If incoherent processes have taken place, the electron will not tunnel back (e).

For nanotubes, because of the $K\,K'$ degeneracy, electrons with the same spin can occupy the same orbital and so this energy difference of the $(0,2)$ singlet and triplet is not present. Therefore, we will use a small magnetic field to split the energies of the different valleys. Without the $K\,K'$ degeneracy, the experiment is the same as for the 'normal' situation.

Following Petta [5], measuring the spin coherence time works as follows:
First, the potential is tilted such that two electrons occupy the right dot and the left dot is empty. After waiting sufficient time, the two-electron state is relaxed to the groundstate $S_{0,2}$ (Fig. 2.6.a). Then, the chemical potentials μ_L and μ_R are aligned such that one electron will tunnel to the left dot and the two electrons occupy the $S_{1,1}$ state (Fig. 2.6.b). Since

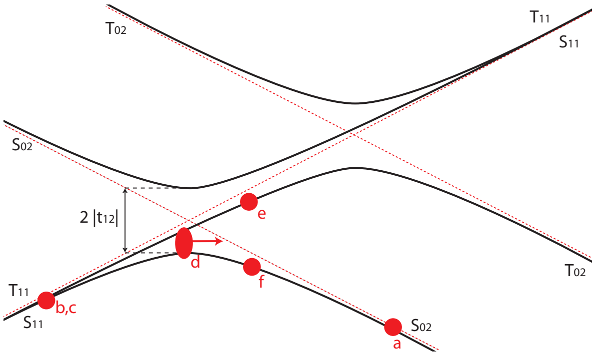

Figure 2.7: Energy diagram corresponding to the double dot spin blockade experiment. The vertical axis corresponds to the energy and the horizontal axis corresponds to gate voltage. The labels *a,b,c,d,e,f* correspond to the labels in Fig. (2.6). t_{12} is the inter-dot coupling. For vanishing coupling, the levels cross (dashed lines). For non-zero coupling, an anti-crossing occurs. The two anti-crossings of the singlet and triplet, corresponding to the transition from $S_{0,2}$ to $S_{1,1}$ and $T_{0,2}$ to $T_{1,1}$, occur at different energies. Due to different spatial configurations, the tunnel coupling at the two anti-crossings can be different. Because the transitions occur at different positions in gate space, the state of the two electrons can be resolved.

the $S_{1,1}$ and $T_{1,1}$ states are degenerate in energy they can mix, due to the interaction with the environment. After some time τ, the potential is tilted back resulting in the situation as illustrated in Fig. 2.6.d. When the two-electron spin state has evolved incoherently during the time τ, the two-electron state is no longer in the $S_{1,1}$ state and the electron cannot tunnel back into the right dot (Fig. 2.6.e). However, if the spin state is still coherent, the $S_{0,2}$ state is accessible and the electron tunnels back (Fig. 2.6.f). The change in charge distribution can be detected using a single electron transistor (SET) [29]. In this way, it is thus possible to infer the information about the spin of an electron by looking at the charge distribution. By varying the waiting time τ the spin coherence time can be resolved.

2.2.2 Quantum dots in carbon nanotubes

For reasons mentioned earlier, the spin of an electron in a carbon nanotube quantum dot is a good candidate for a qubit. One way to create a quantum dot in a carbon nanotube is to simply put two metal electrodes on top of the nanotube: the source and the drain. At the interface of the metal and the semiconducting nanotube a tunnel barrier is formed by the Schottky barrier. The Fermi level of the metal usually does not lie exactly in the middle of the bandgap of the nanotube. Therefore, the formed Schottky barriers are different for electrons than for holes [30]. Usually, hole conductance is better than electron conductance.

Since the finite size of the nanotube between the source and drain quantizes the energy levels, a quantum dot is created in between the barriers. An external gate can be used to tune the energy levels in the quantum dot as described in the previous subsection.

When the external gate voltage is zero, the Fermi energy of the semiconducting nanotube lies inside the bandgap and transport through the nanotube is blocked. By changing the

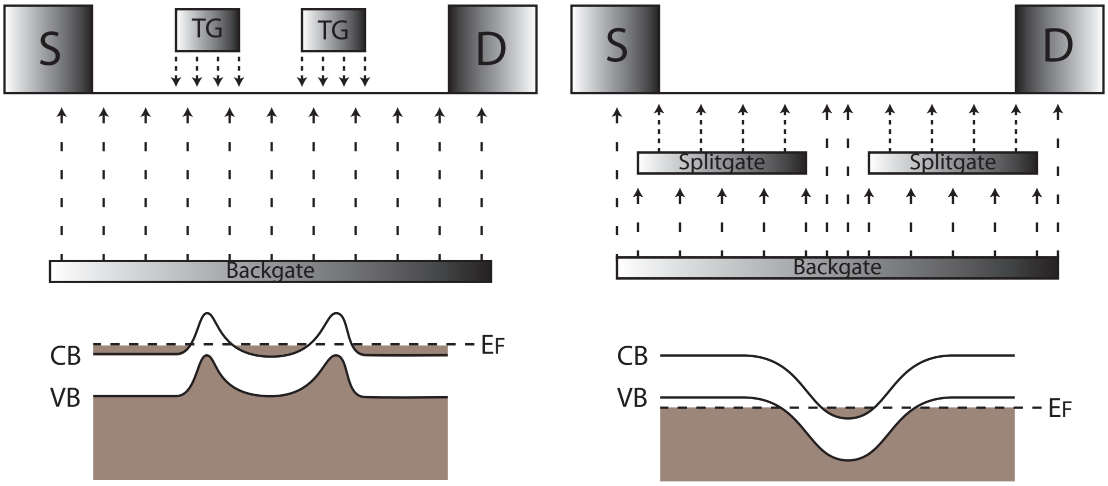

Figure 2.8: Schematic representation of the difference between a device with topgates (TG),(a), and a device with splitgates (b). The arrows represent the field lines from the gates. In a), the barriers are formed underneath the topgates by locally depleting the nanotube. In b), the splitgates are used to electrostatically dope the nanotube with holes (electrons) and the backgate to dope the nanotube with electrons (holes). The barriers are formed at the interfaces of the differently doped regions, which are known as p-n junctions.

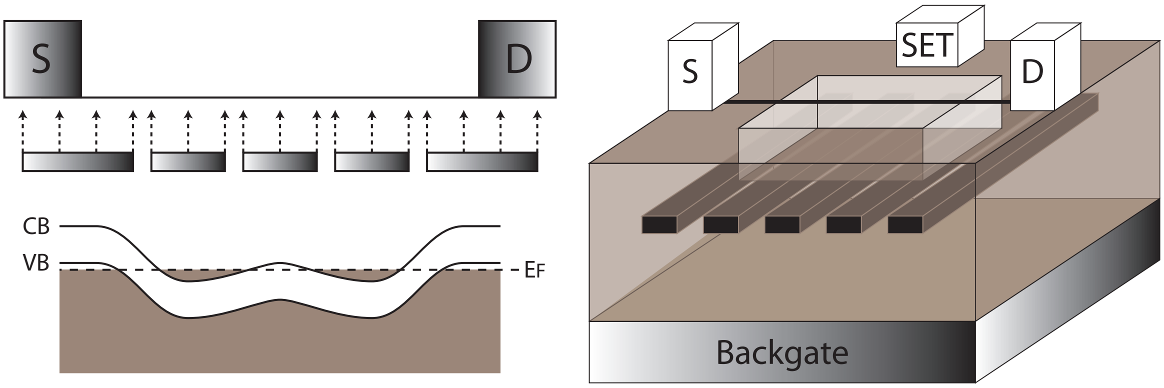

Figure 2.9: Five splitgates are used to make a tunable double dot. Left: The outer two splitgates are used to *p*-dope the nanotube. The other three splitgates make an *n*-type dot, where the middle split gate is used to split the dot into two dots. The backgate is not used. Right: 3D view of a nanotube device with five splitgates. The nanotube is suspended and an SET is used as a charge detector.

gate voltage, it is possible to tune the energy such that the Fermi energy gets inside the valence band, resulting in hole-transport, or inside the conduction band, resulting in electron-transport [10]. It is thus possible to electrostatically dope the nanotube with holes or with electrons (depending on the sign of the gate voltage). The barriers of such a device are formed at the interface of the metal source (and drain) and the semiconducting nanotube. The number of electrons is controlled by a (back) gate. In this way it is, however, not possible to control the width of the barriers. For example in the double dot experiment, tunable barriers are required.

One way to obtain tunable barriers is the use of topgates [13,31–34]. Topgates are placed on top of the nanotube, separated by a layer of a dielectric material. They are positioned relatively close to the nanotube and can therefore be used to form barriers by locally depleting the nanotube. In a topgate device, the two topgates are used to create barriers, and the backgate to change the energy in the dot, see Fig. 2.8. In this way a quantum dot with controllable barriers can be realized.

Another possibility is to use gates positioned underneath the nanotube, called splitgates. In this device the nanotube is locally doped with holes (*p*-type) by the splitgates, and with electrons (*n*-type) by the backgate, resulting in a *p*-*n*-*p* junction. At the interface of the differently doped segments, the Fermi level lies inside the bandgap and the barriers are formed (see Fig.
2.8). It has already been shown that *p*-*n* junctions can be realized with a nearly ideal diode behavior, using two splitgates (without a backgate), [35]. The polarity of the *p*-*n* junction can be switched to *n*-*p* junction, or the device can be used as a *p*- or *n*-channel field effect transistor (FET). The biggest advantage is that this setup allows suspending of the nanotube, avoiding effects of dielectric polarization and trapped charges [36]. Very recent experiments have demonstrated that this technique can be used to make a very clean single electron tunable quantum dot.

In theory, splitgates could also be used to make a double dot (see Fig.
2.9). Aligning five split gates next to each other, the outer two splitgates can be used to *p*-dope the nanotube. The next two splitgates (towards the middle) are used to *n*-dope the nanotube, such that *p*-*n* junctions are formed. Finally, the middle splitgate is used to locally

deplete the nanotube, splitting the dot into two dots. With this setup, we expect that a double dot with tunable barriers can be realized.

2.3 Many body Hamiltonian

The electronic states of the electrons in a quantum dot are described with the many body wavefunction. Analogue to Newton's second law in classical mechanics, the Schrödinger equation describes the space- and time-dependence of a quantum mechanical system.

$$\hat{H}|\Psi\rangle = E|\Psi\rangle \tag{2.26}$$

The solutions of Scrödingers equations are the many body wave functions Ψ which minimize the expectation value of the many body Hamiltonian $\hat{H}$, corresponding to the total energy E of the system. In zero magnetic field, the (static) electronic states of electrons in a fixed external potential are described by the many body Hamiltonian:

$$\hat{H} = \sum_{i=1}^{N} \hat{h}(i) + \frac{1}{2}\sum_{i=1}^{N}\sum_{j=1,j\neq i}^{N} \hat{g}(i,j) \tag{2.27}$$

where $\hat{h}(i)$ is the one-electron operator consisting of the kinetic energy operator and the external potential energy U_{ext}

$$\hat{h}(i) = -\frac{\hbar^2}{2m}\nabla_i^2 + U_{ext} \tag{2.28}$$

and $\hat{g}(i,j)$ is the electron-repulsion operator, describing the Coulomb interaction:

$$\hat{g}(i,j) = \frac{e^2}{r_{ij}} = \frac{e^2}{|r_i - r_j|} \tag{2.29}$$

The many body wavefunction Ψ consist of a spatial part and a spin part. In zero magnetic field, the many body Hamiltonian only operates on the spatial degrees of freedom of the wavefunction and not on the spin degrees of freedom.

We can write the total wavefunction as a product of a spatial part and a spin part, with the Hamiltonian only acting on the spatial part.

$$\Psi_{total} = \Phi_{spatial} \otimes \sigma_{spin} \tag{2.30}$$

The spatial part of the wavefunction is found by solving the eigenvalue problem for the given spinless Hamiltonian. The spin part of the wavefunction corresponds to the eigenfunctions of the Pauli matrices. This statement holds for any number of electrons.

In the next section we will solve the many body Schrödinger equation. Doing so for a large number of electrons results in a partial differential equation with a large number of dimensions, requiring approximations to be made. For a few electrons however, the Schrödinger equation is exactly solvable. We will therefore briefly discuss the case of two electrons here.

The spin states for two electrons are well known. For the spin part of the two-electron wavefunctions, there are four possible spin eigenstates. The spin singlet, S^0, has quantum numbers $s = 0$, $m_s = 0$ and is given by

$$|\sigma_{singlet}\rangle = \frac{1}{\sqrt{2}}(|\uparrow\downarrow\rangle - |\downarrow\uparrow\rangle) \tag{2.31}$$

The spin triplets, T^+, T^0 and T^-, with $s = 1$ and $m_s = +1, 0, -1$ respectively, are given by

$$|\sigma_{triplet}\rangle = \begin{cases} |\uparrow\uparrow\rangle \\ \frac{1}{\sqrt{2}}(|\uparrow\downarrow\rangle + |\downarrow\uparrow\rangle) \\ |\downarrow\downarrow\rangle \end{cases} \tag{2.32}$$

For the spin singlet it holds that interchanging the two electrons results in the spin state $-|\sigma_{singlet}\rangle$, thus it is anti-symmetric. The spin triplet is symmetric. The Pauli principle states that, for fermions, the *total* wavefunction must be anti-symmetric under particle exchange. Therefore, the spin singlet corresponds to a symmetric spatial wavefunction, while the spin triplet corresponds to an anti-symmetric wavefunction. In general, the total wavefunctions (spin plus spatial part), are referred to as the singlet and triplet states. For three or more electrons, the spin states get significantly more complicated. See for example [37].

The anti-symmetrization requirement of the total wavefunction leads to a difference in energy, know as the exchange correlation energy. In the shell filling model, the singlet triplet splitting is given by the level spacing minus this exchange correlation energy. The energy difference can be explained as exchange interaction, which acts like a repulsive force for the anti-symmetric spatial wavefunction, and like an attractive force on the symmetric spatial wavefunction [38]. The double dot experiment as discussed in subsection 2.2.1 is based on controlling this exchange correlation energy.

Chapter 3

Structure of the simulation program

In this chapter we describe the different cornerstones of the simulation program we developed. The goal of the program is to be able to calculate the electronic states of electrons in a quantum dot in a semiconducting nanotube for a given gate geometry and gate voltages. We are especially interested in how we can control these different electronic states. In order to be able to calculate this, we need an approach which covers the multi-scale physics, namely the (macroscopic) electrostatics of the device, as well as the quantum mechanical behavior of the electrons in a quantum dot in the nanotube. We used the method from reference [39] as a guideline.

3.1 Classical electrostatics

3.1.1 The Poisson equation

In electrostatics, the electric potential can be calculated by solving the Poisson equation. The Poisson equation is given by

$$\nabla^2\phi(x,y,z) = -\frac{\rho(x,y,z)}{\epsilon_r\epsilon_0} \tag{3.1}$$

where ϕ is the electrostatic potential, ρ is the charge distribution, ϵ_0 is the permittivity of vacuum and ϵ_r is the relative dielectric constant. For simple problems, such as a parallel plate capacitor, this can be done analytically. However, the devices we want to model often have complex geometries, for which simple analytical equations are no longer sufficient. Fortunately, there are many ways to solve Poisson equation numerically.

To numerically solve the Poisson equation, we first need to project the Poisson equation onto a discrete grid. This results in a set of finite difference equations. Solving these finite difference equations can be done either *directly*, based on matrix multiplications, or *iteratively*, based on relaxation of the electrostatic potential. Iterative methods require much less memory than direct methods, which is why we will use an iterative method. Iterative methods start with an initial guess of the electrostatic potential and then iterate through the grid, replacing the potential with a new value depending on the values of the potential at neighboring points. After sufficient iterations, the solution will be converged, such that the potential satisfies Eq.(3.1).

The simplest relaxation method is the Jacobi method. For a harmonic function holds that its value at a point equals the average of the function around a circle centered about that point. The Jacobi method takes the neighboring points on a square grid and takes the average of those points as the new value for the point under consideration. For a uniform 1D grid with spacing h, the new value of the potential at point i reads

$$\phi_i^{n+1} = \frac{1}{2h^2}(\phi_{i-1}^n + \phi_{i+1}^n) \tag{3.2}$$

Although iterative methods have the advantage of low memory usage, simple relaxation, such as the Jacobi method, is generally a slow process. Fortunately, several well known methods are available to speed up the relaxation. The Gauss-Seidel method, also known as the method of successive displacements, is an improvement on the Jacobi method. It takes already updated points as input, if available, instead of pre-determined values (i.e. from the previous iteration). For a uniform 1D grid, the Gauss- Seidel equation for the new value of ϕ_i reads

$$\phi_i^{n+1} = \frac{1}{2h^2}(\phi_{i-1}^{n+1} + \phi_{i+1}^n) \tag{3.3}$$

The difference with Eq.(3.2) is the replacement of n by $n+1$ for ϕ_{i-1}. It means that, in iteration $n+1$, the electrostatic potential at position $i-1$, which has already been calculated, is used to calculate the new value at point i. In this way the relaxation of the potential is speeded up significantly.

The Gauss-Seidel method improves the speed of the relaxation, but there is yet another method which drastically speeds up the relaxation. Relaxation of the potential can be thought of as information-waves propagating through the system. Since the relaxation depends on neighboring points, errors in short wavelengths are quickly damped. It is, however, the long wavelength fluctuation that is responsible for the slow relaxation. To speed up the diffusion of the information through the system, we use an over-relaxation-method, called successive over-relaxation (SOR). To calculate the new value for the electrostatic potential at a given point, SOR takes the weighted sum of the old and the new solution

$$\tilde{\phi}_i^{n+1} = \phi_i^n + \omega[\phi_i^{n+1} - \phi_i^n] \tag{3.4}$$

which is, for linear systems, guaranteed to converge for $0 < \omega < 2$. For $\omega < 1$ the system is underrelaxed, meaning that the relaxation is damped. For $1 < \omega < 2$ the system is overrelaxed and for $\omega = 1$, the problem reduces to the Gauss-Seidel method. The optimal value of ω, corresponding to the fastest convergence, depends on the size of the system. For a square uniformly spaced grid with $N \times N$ points, the optimal value of ω is given by

$$\omega = \frac{2}{1+\sin(\pi/N)} \approx \frac{2}{1+\pi/N} \tag{3.5}$$

Using the SOR method, Poisson's equation can be solved in a fast way using relatively little memory. However, the usage of memory scales linearly with the number of data points, and therefore the number of data points is limited. The diameter of a nanotube and the typical size of a gate can easily differ two or even three orders of magnitude. Using a uniform grid that is dense enough to accurately calculate the electrostatics of the nanotube in such a device would require a enormous amount of data points. Moreover, we are usually only interested in the electrostatics of specific parts of the device. For these reasons we use a non-uniform grid, which can be very dense around areas we are interested in. For less interesting parts (such as far away from the nanotube, where the electric field lines are zero), large grids pacing can be used.

Non-uniform gridding allows us to load the 3D geometry of relatively large devices into the simulation program, with locally high resolution, using only about 10^7 grid points. For every grid point the type of material is defined, as well as the dielectric constant and the fixed charge. The types of materials can in this case be either an insulator with a fixed charge, or a metal, which corresponds to Dirichlet boundary conditions. For the (metal) gates, the voltages can be set to a specific value.

With the given input described above, we can, in principle, solve the Poisson equation for any given gate geometry. The output contains the potential and electric field lines in all three dimensions, as well as the induced charge on every surface. Since the system is linear, the capacitance between two surfaces can be easily calculated by dividing the induced charge on a surface, due to the voltage of the other surface, divided by this voltage. Written in a more compact form:

$$C_B^A = \frac{Q^A}{\phi_B} \tag{3.6}$$

with C_B^A the capacitance between surface A and surface B. Q^A is the total charge at surface A, induced by the voltage at surface B, ϕ_B. The induced charge Q is calculated using Gauss's law

$$\Phi_s = \int_s \vec{E} \mathrm{d}\vec{s} = \frac{\sum_S q}{\epsilon_r \epsilon_0} = \frac{Q}{\epsilon_r \epsilon_0} \tag{3.7}$$

where Φ_s is the total flux through a closed surface S, $\vec{E}$ is the electric field vector, $\vec{s}$ is the surface vector, and $\sum_S q$ is the sum of the charge inside the closed surface S. For a grid point in rectangular simulation space, the induced charge simply equals the sum of the electric field lines through a rectangular surface around a grid point. The total net charge in the system is zero.

The Poisson solver as described above is very suitable for calculating capacitances between metal surfaces in a realistic device. The effect of different gate geometries can be studied as well as the use of different types of dielectric materials.

3.2 Modeling quantum dots with many electrons

3.2.1 Thomas-Fermi approximation

The Poisson equation as given in the previous section only covers linear systems, i.e. metals and insulators. The final goal of our simulation is to calculate the effect of the change of a gate voltage to the electronic states in a quantum dot in a semiconducting nanotube. This is not possible using the Poisson solver as described until now. For a semiconductor, the charge distribution is a function of the potential, which itself is a function of the charge distribution. Therefore, the Poisson equation becomes non-linear.

$$\nabla^2 \phi(x,y,z) = -\frac{\rho(x,y,z,\phi(x,y,z))}{\epsilon_r \epsilon_0} \tag{3.8}$$

Using a simple Taylor expansion, also the non-linear Poisson equation can be solved iteratively. However, the non-linear Poisson equation with a given charge density functional is no longer guaranteed to converge. For this reason we introduce a new parameter ω_{NL} which is less or equal to unity. In this way we underrelax the potential for those points where the non-linear Poisson equation applies in the same way as we overrelax the linear part [40].

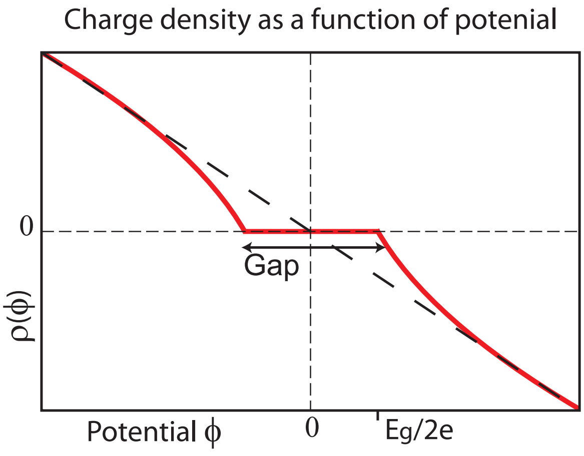

Figure 3.1: Charge density functional of a semiconducting nanotube with a bandgap. Inside the bandgap the density of states is zero and hence there is no charge. The dashed line corresponds to a metallic nanotube.

To be able to solve Eq.(3.8), we need to know what the relation is between ϕ and ρ. If we assume that all quantum numbers are large enough to be treated as a continuum, we use the Thomas-Fermi approximation. In the many electron regime, we can use a charge density functional for the nanotube as an approximation for the ground state electron (or hole) density. The Thomas-Fermi approximation starts with the dispersion relation which we derived in subsection 2.1.1. Rewriting the density of states given by Eq.(2.19) we obtain the charge density functional $\rho(\phi)$.

$$\begin{aligned} \frac{d\rho}{d\phi} &= \frac{edn}{\frac{1}{e}dE} \\ |\rho(\phi)| &= \frac{8e^2}{\sqrt{3}\pi a_0 \gamma_0}\sqrt{\phi^2 - (E_g/2e)^2} \end{aligned} \tag{3.9}$$

where E_g is the energy of the gap of the nanotube. Eq.(3.9) describes how the charge density in the nanotube will vary as a function of the local potential. For $E_g = 0$ the functional becomes linear, corresponding to a metallic nanotube. The functional is plotted in Fig. 3.1. It shows that by applying an external voltage, the nanotube can be electrostatically doped with electrons ($\phi > E_g/2e$) or with holes ($\phi < -E_g/2e$). For zero external voltage, the nanotube is depleted.

As stated before, the Thomas-Fermi approximation assumes that all quantum numbers are large. For the leads of the nanotube, where the Fermi-level is high up (down) in the conduction (valence) band, the Thomas-Fermi approximation holds. Using the Thomas-Fermi approximation to calculate the ground state of the electrons in the dot only makes sense when the number of electrons in the dot is large. For calculating the level splitting for the electrons in the dot however, the Thomas-Fermi approximation is not sufficient.

3.2.2 Hartree approximation

In the Hartree approximation, single electrons are visualized as moving in an effective potential. This allows us to use a single electron Hamiltonian, instead of using the many body Hamiltonian (Eq.2.27). The Schrödinger equation for one electron in the quantum dot in the Hartree approximation is given by

$$\left[-\frac{\hbar^2}{2m^*}\nabla^2 + U_{ext}(r) + e\int \frac{\rho(r')}{|r-r'|}\mathrm{d}r'\right]\psi_i = \epsilon_i\psi_i \tag{3.10}$$

where we use the effective mass m^* given by Eq.(2.14). U_{ext} is the external potential (energy), defined by $U = -|e|\cdot\phi$. In our case the external potential equals the potential due to the charges on the gates (including the image charges of the charges in the dot). The last term between the brackets represents the potential (energy) due to the average charge density distribution $\rho(r')$. Eq.(3.10) has the form of the Schrödinger equation for non-interacting electrons moving in an external effective potential. The eigenfunctions of Eq.(3.10) are the single electron wavefunctions ψ_i.

The square of the modulus of the wavefunctions can be interpreted as smeared out electrons. Using the independent electron model the average charge distribution then reads

$$\rho_i(r) = -|e|\cdot|\psi_i(r)|^2 \tag{3.11}$$

$$\rho_{tot}(r) = -|e|\sum_{i=1}^{N}|\psi_i(r)|^2 \tag{3.12}$$

Combining Eq.(3.10) and Eq.(3.11) yields the final equations, called the Hartree equations:

$$-\frac{\hbar^2}{2m^*}\nabla^2\psi_i(r) + U_{ext}(r)\psi_i(r) + \left[e^2\sum_j\int|\psi_j(r)|^2\frac{1}{|r-r'|}\mathrm{d}r'\right]\psi_i(r) \tag{3.13}$$

The wavefunctions ψ_i depend on the wavefunctions themselves. This means that the Hartree equations are non-linear and therefore they must be solved in an iterative way.

Just like the Thomas-Fermi approximation, the Hartree approximation is a density functional theory since the solution of the Hartree equations depend on a the local charge distribution. However, in contrast to the Thomas-Fermi approximation, it is based on the orbitals of single electrons. From the single electron wavefunctions, the charge distribution is calculated. From the charge distribution, the effective potential is calculated, for which Eq.3.13 is solved. corresponding to a new set of single electron wavefunctions. The new set of single electron wavefunctions results in a new charge distribution and effective potential, and in this way the procedure is repeated until the solution converges. Using the simulation program, the procedure goes as follows:

First, the electrostatic potential is calculated for a given device with given gate voltages. For this calculation we use the Poisson solver with the Thomas-Fermi approximation for the total nanotube. The gate voltages should be chosen such that a quantum dot is formed in the nanotube with well defined barriers between the dot and the leads.

The calculated potential along the nanotube is taken as the initial guess for the effective potential for the electrons in the dot. Since the nanotube is a 1D system, also the effective potential is a 1D potential and so Eq.(3.13) becomes a one dimensional differential equation.

After the initial guess of the effective potential is calculated, we no longer use the Thomas-Fermi approximation for the dot, but we will still use it for the leads (see Fig. 3.2). For the

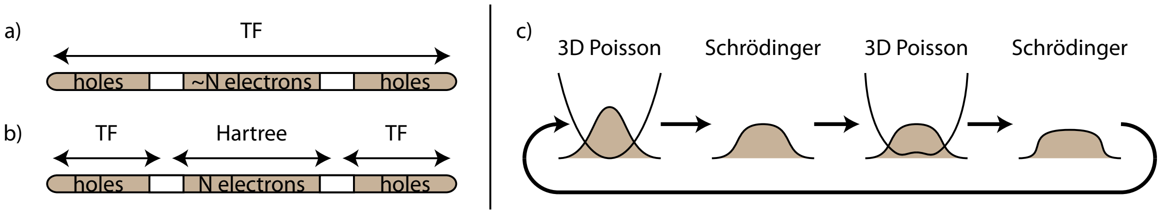

Figure 3.2: Scheme of the method used to calculate Hartree approximation for the electrons in the quantum dot. First, the potential along the nanotube is calculated using the Thomas-Fermi approximation for the total nanotube (a). Then, for the part with the dot the Hartree approximation is used (b). The charge distribution is calculated from the wavefunctions of the single electrons instead of using the Thomas-Fermi density functional. From the charge distribution, the new effective potential is calculated, resulting in a set of wavefunctions. This procedure is repeated until the solution is converged (c).

dot, we will use the Hartree approximation. The tricky point of using the Hartree approximation together with the Thomas-Fermi approximation is what to do with the boundary conditions. We must define the point along the nanotube where we stop using the Thomas-Fermi approximation, and start with the Hartree approximation, i.e. the point where the lead ends and the dot starts. At this point, we use the boundary condition $\psi_i(x_b) = 0$, where x_b is the boundary point for the Thomas-Fermi and Hartree approximation. The most convenient choice for the boundary point is the middle of the barrier, since here also $\rho_{TF}(x_b) = 0$.

The quantum dot in the nanotube is formed by electrostatically doping the nanotube with external gates, so we do not know in advance where exactly the barriers will be. This is the reason why we use the Thomas-Fermi approximation to calculate the initial guess. For systems where the leads and dot are well defined, the position of the barriers are known in advance and this first step is not needed.

As an initial guess for the wavefunctions, we take the wavefunctions of the Thomas-Fermi potential. We could however, take any other initial guess (for example $\psi_i = 0$). The wavefunctions are calculated by applying the Numerov integration method [41], which is very efficient and simple to implement for a 1D problem. From the wavefunctions, the charge distribution is calculated using Eq.(3.12). We can either choose the number of electrons (N), or fill the dot up to the Fermi level. This charge distribution replaces the charge distribution obtained from the Thomas-Fermi approximation. With the new charge, the electrostatic potential is calculated again resulting in a new effective potential. From this effective potential, the new wavefunctions are calculated, which give a new charge distribution, and so on. When the solution converges the self consistent Hartree solution for the dot is found.

3.3 Exact diagonalization for two electrons

Density functional theory (DFT) is based on the density of a uniform, non-interacting degenerate electron gas in a constant potential [42]. For a large number of electrons, this is a good approximation. However, self interaction of the electron which is included, results in large errors when we use the approximation for a small number of electrons. In this section we will discuss a way to correctly solve the many body Hamiltonian for two electrons.

3.3.1 Two-electron Schrödinger equation

For the double dot experiment, we need only two electrons for which DFT is not a good approximation. Fortunately, it is possible to calculate the electronic states for two electrons in a nanotube exactly. Because electrons in a nanotube are strongly confined in the radial direction, a nanotube can be treated as a one dimensional system. The Schrödinger equation, using the Hamiltonian from Eq.(2.27), for two electrons in a one dimensional system reads

$$\hat{H}\Psi(x_1, x_2) = \left[-\frac{\hbar^2}{2m^*}\frac{d^2}{dx_1^2} - \frac{\hbar^2}{2m^*}\frac{d^2}{dx_2^2} + U_{ext}(x_1) + U_{ext}(x_2) + \frac{e^2}{|x_1 - x_2|}\right]\Psi(x_1, x_2) \quad (3.14)$$

where x_1 refers to the spatial degree of freedom of electron 1 and x_2 to that of electron 2. The last term between the brackets is the Coulomb interaction term, which models the interactions and correlations between the two dot-electrons (this term is also known as $\hat{g}_{12}$). For a one dimensional system with two electrons, the Schrödinger equation is a two dimensional differential equation with variables x_1 and x_2. Such a differential equation is exactly solvable.

3.3.2 Visualizing the two-electron problem

Solving the eigenvalue problem for *two* electrons in *1D* space is very similar to the case with *one* electron in *2D* space. In both cases a two dimensional differential equation is solved to obtain two dimensional wavefunctions. There are however, some important differences.

The first difference regards the potential seen by the electron(s). In Eq.(3.14) there is an external potential for each electron. By defining

$$\bar{U}_{ext}(x_1, x_2) = U_{ext}(x_1) + U_{ext}(x_2) \quad (3.15)$$

we get an effective 2D potential for the two electrons. For both electrons, the external potential U_{ext} is, of course, equal. Therefore the given effective external potential $\bar{U}_{ext}(x_1, x_2)$ is restricted by symmetry conditions, which is not the case for one electron in 2D space.

The Coulomb interaction term can also be thought of as an effective 2D potential seen by the two electrons. Coulomb interaction is dependent on the distance between electrons. For two electrons in free space it yields

$$V_C(x_1, x_2) = V_C(|x_1 - x_2|) = \frac{e^2}{4\pi\epsilon_r\epsilon_0|x_1 - x_2|} \quad (3.16)$$

This 2D potential represents the potential at point x_1, due to a charge at point x_2. The 2D Coulomb 'potential' is maximal along the line $x_1 = x_2$ in the two dimensional parameter space, since here the repulsion is the highest.

Putting everything together, the total effective 2D potential for the two electrons in the 1D nanotube becomes

$$U^*_{ext}(x_1, x_2) = U_{ext}(x_1) + U_{ext}(x_2) + V_C(x_1, x_2) \quad (3.17)$$

and the eigenvalue problem is equivalent to the case with one electron in 2D space, with an external potential U^*_{ext}. An example of the effective 2D external potential U^*_{ext} is illustrated in Fig. 3.3.

The second difference from the two dimensional single electron case, is the interpretation of the wavefunctions. The two electrons see an effective two dimensional potential, for which

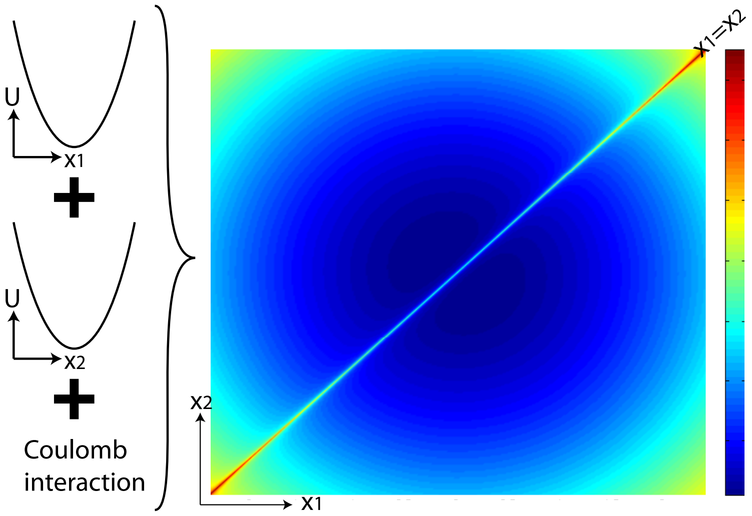

Figure 3.3: Visualization of an example of the 2D potential for the two-electron wavefunction: $U^*_{ext}(x_1, x_2) = U_{ext}(x_1) + U_{ext}(x_2) + V_C(x_1, x_2)$. For this example, the 1D external potential is an harmonic oscillator potential. The Coulomb interaction is maximum at the line $x_1 = x_2$. For $V_C = 0$ the problem reduces to that of two independent electrons, which is exactly equivalent to the eigenvalue problem for one electron in 2D potential.

the corresponding wavefunctions are found. For the 2D single electron case, the modulus square of the wavefunction represents the probability of finding the electron at a given space interval in the two dimensional space. For the one dimensional, two electron case, this is different.

The modulus squared of the two-electron wavefunction represents the conditional probability of finding electron one at a x_1, given that electron two is at position x_2 (x_1 and x_2 correspond to a one dimensional space interval). Since the electrons are identical particles, interchanging x_1 and x_2 gives the same result.

$$|\Phi(x_1, x_2)|^2 = P(x_1|x_2) = P(x_2|x_1) \tag{3.18}$$

The charge distribution for electron one is found by integrating the modulus squared of the wavefunction over the spatial degree of freedom of electron two. Again, since the electrons are identical particles, integrating over x_1 results in the same charge distribution as integrating over x_2. The total charge density is obtained by adding the two single electron charge distributions.

$$\begin{aligned} \rho_1(x_1) &= e \int |\Phi(x_1, x_2)|^2 \mathrm{d}x_2 \\ \rho_2(x_2) &= e \int |\Phi(x_1, x_2)|^2 \mathrm{d}x_1 = \rho_1(x_2) \end{aligned} \tag{3.19}$$

$$\rho_{tot}(x) = \rho_1(x) + \rho_2(x) \tag{3.20}$$

where x is the spatial coordinate at the 1D nanotube.

As discussed before, the total wavefunction must be anti-symmetric under particle exchange. Therefore, the spin singlet corresponds to a symmetric spatial wavefunction and

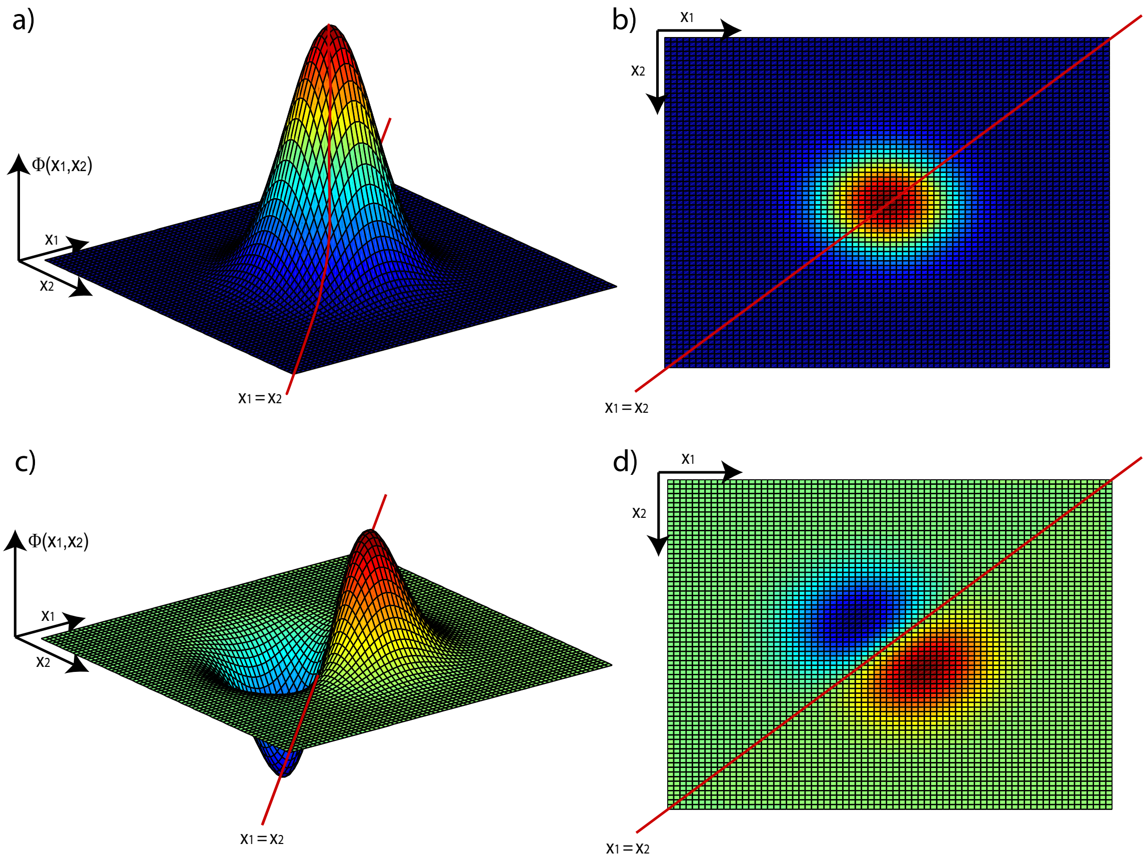

Figure 3.4: Spatial part of the two-electron wavefunction $\Phi(x_1, x_2)$ for a 1D system. In a) (3D view) and b) (top view) the spatial wavefunction with the lowest energy is plotted. The wavefunction is symmetric about the line $x_1 = x_2$ and corresponds to the spin singlet. The spatial wavefunction corresponding to the spin triplet has a node at $x_1 = x_2$ and is anti-symmetric (c,d). Integrating the square modulus of the wavefunction over one of the two degrees of freedom results in the charge density along the nanotube.

the triplet to a anti-symmetric spatial wavefunction. Symmetry under particle exchange in this context can be visualized by the mirror symmetry of the wavefunctions about the line $x_1 = x_2$, see Fig. 3.4.

For the double dot case, there are four states we are interested in. The $S_{0,2}$ and $T_{0,2}$ are the singlet and triplet states, corresponding to the case with two electrons in one dot. These states are expected to look similar to the singlet and triplet states given in Fig. 3.4. The singlet and triplet states corresponding to the case with one electron in each dot are the $S_{1,1}$ and $T_{1,1}$ states. When the electrons are in either one of these states, they are separated spatially. They are however, strongly correlated and therefore should be thought of as a two-electron state, coherently distributed over both dots.

3.3.3 Calculating the potentials

The two-electron wavefunction of the electrons in the dot depends on the external potential U_{ext}, which again depends on the electrons in the dot. In the Hartree approximation we solved this in an iterative way, where we calculated the new effective potential with the charge distribution obtained from the wavefunctions. However, we included the electric field from the electrons in the dot themselves when we calculated the new potential.

The external potential U_{ext} from Eq.(3.14) represents the potential due to all electrons outside the dot, including the image charges of the dot. However, in contrast to the Hartree approximation, the interaction and correlation of the two electrons in the dot is modeled with the Coulomb term $V_C(x_1, x_2)$. For this reason we need to calculate the potential due to all charges in the system but the electrons in the dot. We do this in the following way:

First, the initial guess for the charge distribution in the dot is calculated. The most convenient way to do this is to take the charge distribution from the Thomas-Fermi solution for the nanotube. The system then contains the amount of image charges equal to the number of electrons in the dot. The potential at the nanotube however, includes the electric field from the electrons in the dot which must be excluded. To calculate the correct potential, all charges in the system are fixed, and the charge in the dot is removed ($\rho_{dot}(\phi) = 0$). Then the 3D Poisson equation is solved again resulting in a potential along the nanotube corresponding to the external potential U_{ext}. This potential is called the bare potential.

After the bare potential is calculated, the Schrödinger equation is solved resulting in a new two-electron wavefunction with a new charge distribution. This charge distribution is plugged into the simulation program and the 3D electrostatics are again calculated. Next all charges are kept fixed, the charge in the dot is removed, and the new bare potential is calculated. The change of the charge distribution in the dot results in a change of the charge distribution at the gates and leads, which again results in a new bare potential. In this way, the Schrödinger equation is solved iteratively.

In the iterative Schrödinger solving process, the redistribution of the charge in the dot results in a redistribution of the image charges, which again results in a change in the external potential. Since the image charges are relatively far away (at the gates and leads), we neglect the change in the external potential because of the redistribution of the electrons in the dot [1]. By neglecting the change in the external potential, the iterative process is reduced such that only two 3D electrostatic calculations are needed. One to obtain the initial guess, and one to get the exact number of image charges (in contrary to the way the charge is distributed, the exact amount of image charges is relevant).

The interaction of the electrons in the dot with all charges outside the dot is modeled with the mean field approximation, captured in U_{ext}. What is crucial in this approach is that self interaction of the electrons in the dot is excluded. The interaction and correlation of the two electrons in the dot can now be modeled with the Coulomb interaction term.

The Coulomb interaction term as given in Eq.(3.16) diverges for a 1D system for $x_1 = x_2$. Although the nanotube is a 1D system, it does have a finite size in the radial direction. For this reason we can add a form factor μ that softens the Coulomb potential [43]. Using the form factor, the analytical expression for the Coulomb interaction becomes:

$$V_C(x_1, x_2) = \frac{e^2}{4\pi\epsilon_r\epsilon_0\sqrt{(x_1 - x_2)^2 + \mu^2}} \tag{3.21}$$

One approximation is to take μ to be equal to the radius of the nanotube. However, the two dimensional Coulomb potential represents the potential at point x_1, due to a charge

---

[1] In DFT, this approximation can not be applied since the external (effective) potential depends directly on the electrons in the dot.

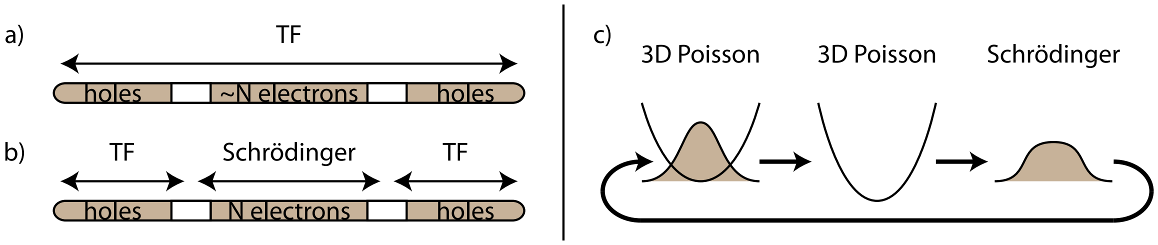

Figure 3.5: Scheme of the iterations needed for solving the two electron Scrödinger equation. a: First a Thomas-Fermi approximation for the total nanotube is used. b: Then, the Schrödinger equation is used for the dot and the Thomas-Fermi approximation is used for the leads only. c: At every iteration, the 3D electrostatics are calculated twice. Once to calculate the new charge distribution at the gates and leads, and once in the bare potential. Then the two-electron wavefunction is calculated resulting in a new charge distribution of the two electrons in the dot, which results in a new charge distribution at the gates and leads and so on.

at point x_2 and it can therefore also be calculated using the Poisson solver. To do this, an amount of charge is placed on position x_1 at the nanotube and the potential along the nanotube due to this charge is calculated, by solving the 3D Poisson equation. This is done for every point along the nanotube, resulting in a 2D screened Coulomb interaction potential. In this way, the screening of the charge at the gates and the leads is included in the Coulomb interaction of the electrons in the dot.

In Fig. 3.6, a 1D cut of the 2D Coulomb interaction 'potential' is plotted for three cases: The unscreened Coulomb interaction without a form factor diverges for $x_1 = x_2$ (Eq.(3.16). Using a form factor of $\mu = 0.5\,\text{nm}$, the Coulomb interaction has a cut off and its maximum is $V_{C_{x_1=x_2}} = 2.88\,\text{eV}$. For $x_1 \neq x_2$, the Coulomb interaction equals the unscreened Coulomb interaction without a form factor.

The screened Coulomb interaction calculated using the Poisson solver is different from the unscreened Coulomb interaction. The screening from the gates causes the Coulomb interaction fall off faster for a large distance. Also, the maximum of at $x_1 = x_2$ is $V_{C_{x_1=x_2}} = 0.82\,\text{eV}$, which is significantly lower than for the unscreened Coulomb interaction. This difference does not come from the gates, but from the silicon oxide the nanotube is lying on. The polarization of the silicon oxide reduces the electric field inside the dielectric material, and thus it reduces the Coulomb interaction of the electrons at the nanotube. For a suspended nanotube, the value of the Coulomb interaction at $x_1 = x_2$ is $V_{C_{x_1=x_2}} = 1.91\,\text{eV}$.

3.3.4 Solving the discretized two-electron Schrödinger equation

To solve the two dimensional Schrödinger equation, we project the Hamiltonian onto a discretized mesh, just like we did for the Poisson equation. For a uniformly discretized mesh with spacing Δx, the second derivative equation reads

$$f''(x) = \frac{f(x_{i-1}) - 2f(x_i) + f(x_{i+1})}{\Delta x^2} \tag{3.22}$$

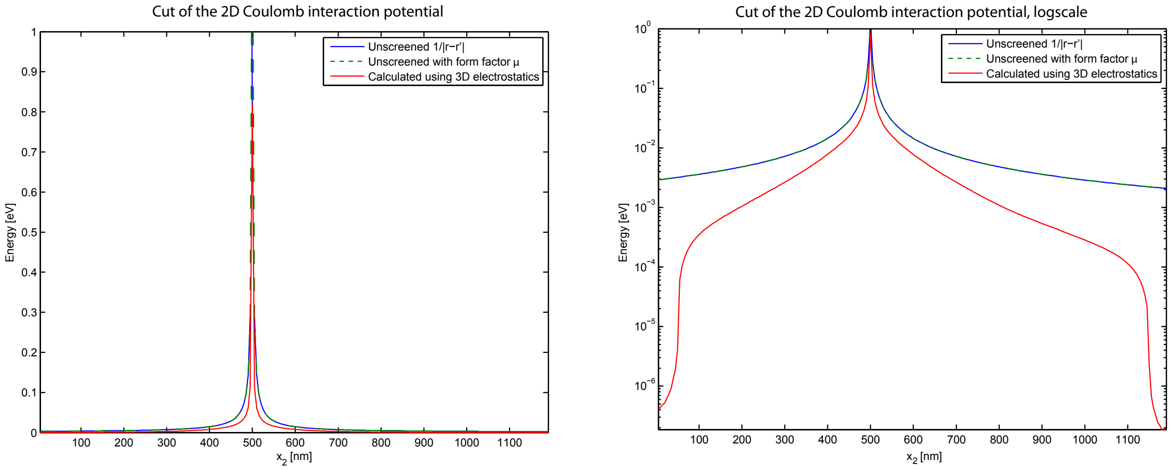

Figure 3.6: Cut of the 2D Coulomb interaction 'potential' at $x_1 = 500\,\mathrm{nm}$ plotted on a linear scale (left) and on a logarithmic scale (right). The unscreened Coulomb interaction can be softened by using a form factor μ, resulting in a cutoff at $x_1 = x_2$. The screened Coulomb potential is calculated using the 3D Poisson solver. The gates and leads are included in the calculations. For larger distances, the Coulomb interaction is strongly screened by the gates and leads (and source and drain). For smaller distances, the dielectric material underneath the nanotube also reduces the Coulomb interaction.

Applying this to the Schrödinger equation yields

$$\begin{aligned}\hat{H}\Phi(x1_i, x2_j) = &-\frac{\hbar^2}{2m^*\Delta x^2}\left[\Phi(x1_{i-1}, x2_j) - 2\Phi(x1_i, x2_j) + \Phi(x1_{i+1}, x2_j)\right] \\ &-\frac{\hbar^2}{2m^*\Delta x^2}\left[\Phi(x1_i, x2_{j-1}) - 2\Phi(x1_i, x2_j) + \Phi(x1_i, x2_{j+1})\right] \\ &+\left[\,U_{ext}(x1_i) + U_{ext}(x2_j) + V_C(x1_i, x2_j)\,\right]\ \Phi(x1_i, x2_j)\end{aligned} \tag{3.23}$$

We only take the spatial part of the total wavefunction into account, since we use a spinless Hamiltonian. In order to solve the Schrödinger equation, we rewrite it into a matrix form. The easiest way to do this is to write the wavefunction $\Phi(x_1, x_2)$ as a 1D array, using a new index

$$k = j + (i-1)L \tag{3.24}$$

The 1D representation of the 2D wavefunction then becomes

$$\tilde{\Phi}_k = \Phi(x1_{(i-1)L}, x2_j) \tag{3.25}$$

where L is the number of datapoints taken along the nanotube. The length of the 1D array $\tilde{\Phi}_k$ thus equals L^2. For the Coulomb interaction term $V_C(x_1, x_2)$ we can do the same, yielding

$$\tilde{V}_{C_k} = V_C(x1_{(i-1)L}, x2_j) \tag{3.26}$$

and for the external potential we get

$$\tilde{U}_{ext_k} = U_{ext}(x1_{(i-1)L}) + U_{ext}(x2_j) \tag{3.27}$$

Using this representation, the Schrödinger equation can be written as a matrix of size $L^2 \times L^2$. Every diagonal element corresponding to different indices i and j:

$$\begin{aligned} \alpha_{k,k} &= [\frac{\hbar^2}{m^* \Delta x_1^2} + \frac{\hbar^2}{m^* \Delta x_2^2} + \tilde{U}_{ext_k} + \tilde{V}_{C_k}]\tilde{\Phi}_k \\ &= \\ \alpha_{k,k} &= [\frac{\hbar^2}{m^* \Delta x_1^2} + \frac{\hbar^2}{m^* \Delta x_2^2} + U_{ext}(x_{1_{(i-1)L}}) + \\ &\quad + U_{ext}(x_{2_j}) + V_C(x_{1_{(i-1)L}}, x_{2_j})]\Phi(x_{1_{(i-1)L}}, x_{2_j}) \end{aligned} \tag{3.28}$$

The four off-diagonal elements correspond to either $\Phi(x_{1_{i+1}}, x_{2_j})$, $\Phi(x_{1_{i-1}}, x_{2_j})$, $\Phi(x_{1_i}, x_{2_{j+1}})$ or $\Phi(x_{1_i}, x_{2_{j-1}})$:

$$\begin{aligned} \beta_{k,k+1} &= -\frac{\hbar^2}{2m^* \Delta x_2^2}\tilde{\Phi}_{k+1} = -\frac{\hbar^2}{2m^* \Delta x_2^2}\Phi(x_{1_{(i-1)L}}, x_{2_{j+1}}) \\ \beta_{k,k-1} &= -\frac{\hbar^2}{2m^* \Delta x_2^2}\tilde{\Phi}_{k-1} = -\frac{\hbar^2}{2m^* \Delta x_2^2}\Phi(x_{1_{(i-1)L}}, x_{2_{j-1}}) \\ \beta_{k,k+L} &= -\frac{\hbar^2}{2m^* \Delta x_1^2}\tilde{\Phi}_{k+L} = -\frac{\hbar^2}{2m^* \Delta x_1^2}\Phi(x_{1_{(i)L}}, x_{2_j}) \\ \beta_{k,k-L} &= -\frac{\hbar^2}{2m^* \Delta x_1^2}\tilde{\Phi}_{k-L} = -\frac{\hbar^2}{2m^* \Delta x_1^2}\Phi(x_{1_{(i-2)L}}, x_{2_j}) \end{aligned} \tag{3.29}$$

Putting everything together results in a five-diagonal matrix of size $L^2 \times L^2$. It may be obvious that for a reasonable number of data points along the nanotube, the Schrödinger matrix can get very large. Solving the eigenvalue problem for such a matrix requires a lot of memory and computational power. Fortunately, the matrix is sparse and can be solved easily using a method called the Lanczos method [41]. The Lanczos method is a well known, iterative method which converges to the lowest (or highest) eigenvalue of a sparse matrix. Using the Lanczos method, we can choose to calculate only a few lowest eigenvalues and eigenvectors, instead of calculating the complete spectrum. The wavefunction with the lowest energy corresponds to the spin singlet, and the second lowest to the spin triplet. For the double dot case near to the anti-crossing (see Fig. 2.7), the four lowest states are the $(0, 2)$ and $(1, 1)$ singlet and triplet states.

Just as in the real double dot experiment, the external potential in the simulation is changed by changing the voltages at the gates only. The energies of the four states are calculated for the corresponding gate voltages and an energy diagram as illustrated in Fig. 2.7 is found. In this energy diagram, the full 3D geometry of the device is taken into account, screening of the gates and leads is included, and the energies and wavefunctions of the electrons are the exact solutions of the two-electron Schrödinger equation.

Chapter 4

Simulation results

4.1 Classical electrostatics

In this section we will present the results of classical electrostatics simulations. Before we started working on these simulations, the program was thoroughly tested by comparing simulation results with known solutions. Among these we compared the output with the simple parallel plate capacitor, the wire to plane model, as well as experimental data [44,45]. All simulation results were in good agreement. In the next subsection we give an example of relevant simulations done for a realistic nanotube device.

4.1.1 Capacitive coupling between an SET and a suspended nanotube

Suspending a nanotube in a device avoids the unwanted effects from trapped charges in the oxide layer. However, doing so may result in changes in capacitive coupling of the nanotube to other parts of the device. In the newest generation of nanotube devices, an SET is used as a charge detector [29]. It is therefore important to know if, and how, capacitive coupling between the nanotube and the SET changes by suspending the nanotube.

The capacitance between the SET island and a metallic nanotube is given by

$$C_{SET}^{NT} = \frac{Q^{NT}}{V_{SET}} = \frac{Q^{SET}}{V_{NT}} = C_{NT}^{SET} \tag{4.1}$$

where Q^{NT}, Q^{SET} is the total charge at the nanotube and SET island respectively, and V_{SET}, V_{NT} is the voltage at the SET or nanotube (see Eq.(3.6)). The total capacitances, or self capacitances of the nanotube and SET island are given by

$$C_{\Sigma}^{NT} = \frac{Q^{NT}}{V_{NT}} \tag{4.2}$$

$$C_{\Sigma}^{SET} = \frac{Q^{SET}}{V_{SET}} \tag{4.3}$$

For the charge detection, it is important to have a good coupling between the SET and the dot in the nanotube. The coupling from the dot to the SET can be determined by calculating the amount of charge at the SET, induced by an amount of charge in the dot. From Eq.(4.1) and Eq.(4.2) the induced charge at the SET due to a charge at the nanotube follows

$$Q^{SET} = \frac{C_{SET}^{NT}}{C_{\Sigma}^{NT}} Q^{NT} \tag{4.4}$$

In the same way, using Eq.(4.1) and Eq.(4.3), the charge at the nanotube due to the charge at the SET yields

$$Q^{NT} = \frac{C^{NT}_{SET}}{C^{SET}_{\Sigma}} Q^{SET} \tag{4.5}$$

The latter coupling is unwanted coupling of the SET to the nanotube, which is called the back-action.

Ideally, an electron entering the dot in the nanotube induces as much as possible (positive) charge at the SET. From Eq.(4.4) it is clear that the capacitance between the SET and nanotube should therefore be large, compared to the total capacitance of the nanotube (of course $C^{NT}_{\Sigma} \geq C^{NT}_{SET}$). The back-action, defined by Eq.(4.5), should be low. For this reason, the self capacitance of the SET should be relatively large.

The capacitances are calculated using the developed simulation program and the effect of suspending the nanotube is studied. The simulation is performed for a device with a suspended nanotube, and for the same device, but without suspending the nanotube. In the simulation program, we use a metallic nanotube which can be represented as a line with a

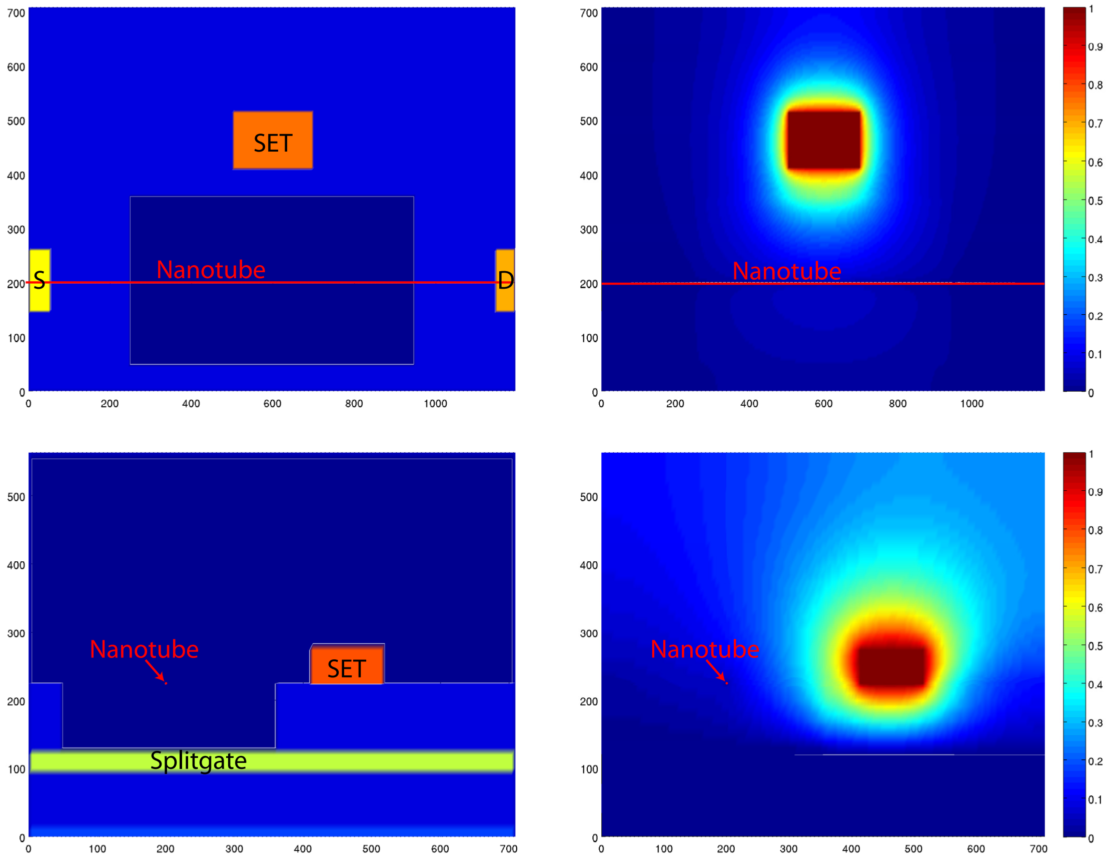

Figure 4.1: Topview (upper) and sideview (lower) of the device from Fig. 2.9 with a suspended nanotube and a simplified charge detector (SET) as loaded into the simulation program. The distances given on the axis are in units nm. The voltage at the SET island is set to 1 V and the electrostatic potential is calculated (right). From the electrostatic potential, the capacitances are calculated.

width and height of one pixel (1 nm). Furthermore, the device includes five splitgates as illustrated in Fig. 2.9, a source and drain, and a simplified SET. The device is loaded into the simulation program, and the electrostatics are calculated (see Fig. 4.1).

The nanotube is divided in three segments. The middle segment of the nanotube is called NT_{dot} and is 500 nm long (the total suspended part is 700 nm). This is the part where the dot will be made. The capacitances between the SET and the nanotube are calculated for this segment. Also the self capacitances are calculated. The results of the simulations are given in table 4.1.

Table 4.1 shows that the capacitance between the SET and the nanotube decreases when the nanotube is suspended. However, the coupling and back-action also depend on the self capacitances, which are also decreased. Table 4.2 shows the coupling and back-action to the dot.

Suspending the nanotube results in a significant increase of the coupling of the SET to the part of the nanotube with the dot. At the same time, the back-action is decreased. The ratio between the coupling and back-action is increased from a factor 2.15 to 5.09 for the dot.

From Eq.(4.5), it would seem that having a large self capacitance for the SET would be ideal. In real devices however, the charge in the nanotube is not detected by looking at the amount of charge at the SET, but by measuring the current through the SET. The magnitude of the current oscillations through the SET gets smaller for smaller charging energy, $E_C = e^2/2C_\Sigma^{SET}$, resulting in a lower overall sensitivity. The results of the simulations show that the back-action is decreased for a suspended nanotube, but at the same time the self capacitance of the SET is also slightly decreased. Therefore, the overall sensitivity of the SET is slightly increased.

	Non-suspended	Suspended	Rel. change	
$C_{NT_{dot}}^{SET}$	$4.27 \cdot 10^{-1}$ aF	$3.49 \cdot 10^{-1}$ aF	-0.18	Capacitance SET to dot
C_Σ^{SET}	$2.28 \cdot 10^{1}$ aF	$2.21 \cdot 10^{1}$ aF	-0.03	Self capacitance SET
$C_\Sigma^{NT_{dot}}$	$1.06 \cdot 10^{1}$ aF	4.33 aF	-0.59	Self capacitance dot

Table 4.1: Simulation results for a device with a suspended nanotube and one with a non-suspended nanotube. For the device with the suspended nanotube, the calculated capacitances are lower.

	Non-suspended	Suspended	Rel. change	
$C_{SET}^{NT_{dot}}/C_\Sigma^{NT_{dot}}$	0.040	0.081	$+1.00$	Coupling, dot
$C_{NT_{dot}}^{SET}/C_\Sigma^{SET}$	0.019	0.016	-0.15	Back-action, dot
$C_\Sigma^{SET}/C_\Sigma^{NT_{dot}}$	2.15	5.09	$+1.36$	Coupling/back-action, dot

Table 4.2: Simulation results for a device with a suspended nanotube and one with a non-suspended nanotube. Suspending the nanotube results in higher coupling to the nanotube and lower back-action.

The simple simulations we did give us a qualitative picture of the capacitive changes between the SET and the nanotube. All together, the results of the simulations are that suspending the nanotube gives a better coupling of the dot to the SET. Also, the back-action is lower for a suspended nanotube, and the overall sensitivity of the SET is slightly increased.

More relevant results from the 3D Poisson simulations can be found in reference [29] and [46].

4.2 Quantum dots with many electrons

The capacitances calculated in the previous section are those of a system with a metallic nanotube. For the double dot experiment, we will need a semiconducting nanotube. The Thomas-Fermi approximation can be used to model semiconducting materials.

4.2.1 Controlling quantum dots in semiconducting nanotubes

In this subsection we will discuss two devices which could be used to make a dot with tunable barriers in a semiconducting nanotube. One device uses topgates to locally deplete the nanotube. In the other device splitgates are used and barriers are formed by *p*-*n*-junctions. The devices are illustrated in Fig. 2.8.

For the simulations, we use a device with two topgates which has a silicon oxide layer of 285 nm between the nanotube and the backgate. The topgates are separated from the nanotube by an oxide layer of 20 nm and the topgates themselves are 30 nm high. For the splitgate device, the distance between the splitgates and backgate is 285 nm. The two splitgates are 50 nm thick and on top of the split gates is another 100 nm of silicon oxide on which

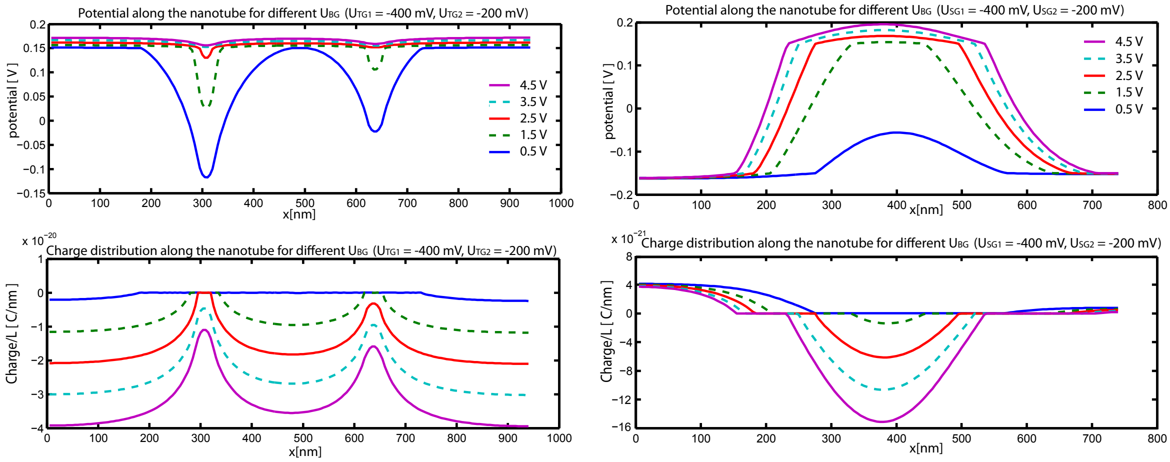

Figure 4.2: 1D potential and charge per unit length along the nanotube for two different devices for different backgate voltages. Left: topgates are used to locally deplete the nanotube such that in between a dot is formed. For a low backgate voltage ($V_{BG} \leq 0.5\,\mathrm{V}$), the nanotube is depleted in between the topgates and thus there is no dot. For high backgate voltage ($V_{BG} \geq 3.5\,\mathrm{V}$) the nanotube is no longer depleted underneath one or more topgates. For this range of voltages, only for $V_{BG} = 1.5\,\mathrm{V}$ a dot is formed. Right: Splitgates pull the valence band above the Fermi level and barriers are formed by *p*-*n*-junctions. For $V_{BG} \geq 1.5\,\mathrm{V}$, a dot is formed.

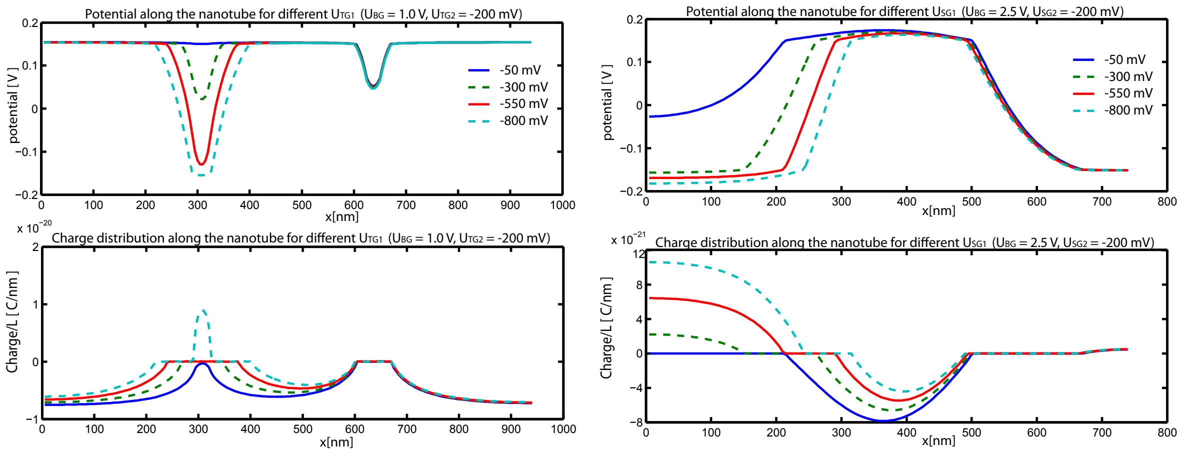

Figure 4.3: 1D potential and charge per unit length along the nanotube for the topgate device (left) and the splitgate device (right). Only the voltage at the left gate (topgate or splitgate) is changed. Left: The width of the depletion region can be controlled by the voltage applied to the topgate. For a high topgate voltage, a second (p-type) dot is formed below the topgate. Right: changing the splitgate voltage changes the width of the depletion region and also shifts its position.

the nanotube lies. The total distance between the nanotube and the backgate is 450 nm. The horizontal distance between the topgates as well as between the splitgates is 300 nm. In the simulation we use the Thomas-Fermi approximation as given in subsection 3.2.1 to model the electronic properties of the nanotube. The bandgap of the nanotube is chosen to be $E_g = 300\,\mathrm{meV}$.

We calculate the electrostatic potential for different voltages applied to the gates to find the effect on the barriers and the dot. To do this, one gate (topgate, respectively splitgate) is set to $-200\,\mathrm{mV}$ and the voltage of the second gate and the backgate are swept. Ideally, the barriers are controlled with the topgates or splitgates, and the backgate is used to control the number of electrons in the dot. First we keep the right gate fixed at $-200\,\mathrm{mV}$ and the left gate at $-400\,\mathrm{mV}$ and calculate the 3D electrostatic potential for different backgate voltages. In Fig. 4.2 the electrostatic potential and corresponding charge distribution is plotted for different backgate voltages.

For the topgate device with the give topgate voltages, there is no dot formed for $V_{BG} \leq 0.5\,\mathrm{V}$. For this backgate voltage, the Fermi level lies in the bandgap for the part in between the topgates, and therefore the nanotube is here depleted. For a high backgate voltage $V_{BG} \geq 2.5\,\mathrm{V}$, the nanotube is no longer depleted underneath the topgates, i.e. the barriers vanish. The barriers are formed by by compensating the electric field from the backgate with the topgates. Therefore, the width of the barrier is does strongly depend on the backgate voltage.

In the splitgate device there is also no dot formed for $V_{BG} \leq 0.5\,\mathrm{V}$. In contrast with the topgate device however, the barriers will not vanish for higher backgate voltages. Increasing the backgate results in a larger dot, and the barriers are shifted in position instead of being reduced.

Next we sweep one of the topgates and one of the sidegates, keeping the voltage at the backgate and the other gates fixed. The calculated potentials and charge distributions are

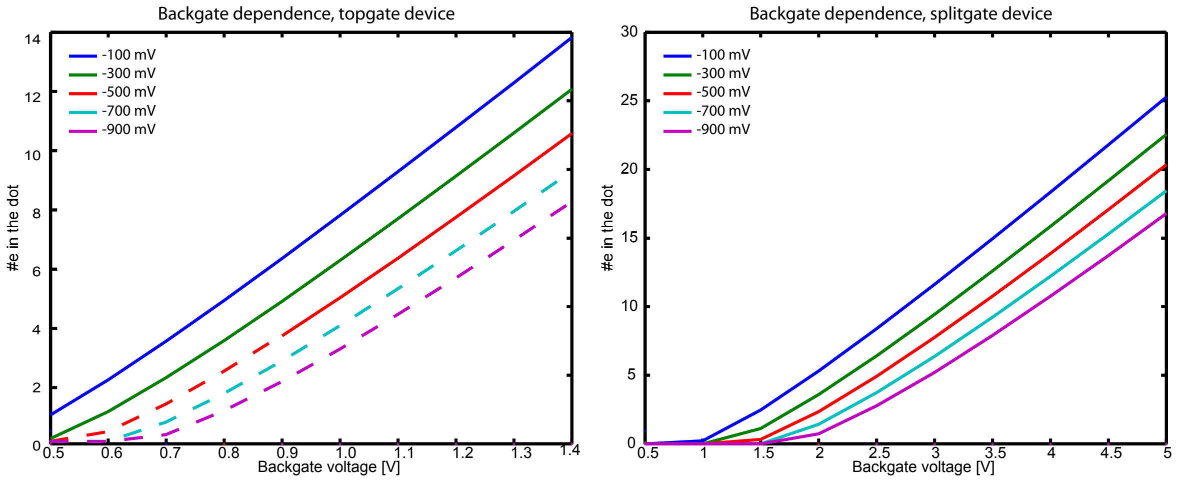

Figure 4.4: Dependence of the number of electrons in the dot versus backgate voltage. The capacitance between the backgate and nanotube, given by the slopes of the lines, is higher for the topgate device. The dashed line corresponds with the case where an extra p-type dot underneath the topgate is formed.

plotted in Fig. 4.3. For the given backgate voltage, there is no barrier for $V_{TG} = -50\,\mathrm{mV}$. Increasing the topgate voltage increases the barrier width and decreases the dotsize. However, at topgate voltage of $V_{TG} \leq -800\,\mathrm{mV}$, the valence band is pulled above the Fermi level and a *p*-type dot is formed under the topgate.

Splitgates completely screen the electric fieldlines from the backgate. When the voltage at the splitgates is small enough, the part of the nanotube screened by the splitgates is depleted. Fig. 4.3 shows that for $V_{SG} \geq -50\,\mathrm{mV}$, the nanotube lying above the left splitgate is completely depleted. For higher (negative) splitgate voltage, this part of the nanotube is doped with holes and the width of the barrier is decreased.

The number of electrons will in both devices be controlled with the backgate. Fig. 4.4 shows the number of electrons as a function of the backgate voltage. The capacitances of the gates to the dot are given by the slopes of Fig. 4.4. For the splitgate devices, the number of electrons depends linearly on the backgate voltage when five or more electrons are in the dot. For this region the capacitance is $C^{BG}_{NT_{dot}} = 0.9 - 1.1\,\mathrm{aF}$. For the topgate device, the capacitance is $C^{BG}_{NT_{dot}} = 1.7 - 2.5\,\mathrm{aF}$ for $0.5\,\mathrm{V} \leq U_{BG} \leq 2\,\mathrm{V}$. For a backgate voltage higher than $V_{BG} = 2\,\mathrm{V}$, the barriers vanish. The large difference in the capacitance for the two devices is a result of the splitgates screening the electric fieldlines from the backgate. Also, the capacitance of the backgate depends on the voltage at the other gates.

The width of the barriers between the dot and the leads is controlled with the topgates or splitgates. However, the number of electrons also depends on the voltages applied to these gates. Moreover, for a high topgate voltage, it can happen that a second dot is created underneath the topgate. In Fig. 4.5, the with of the (left) depletion region is plotted versus the topgate and splitgate voltage, together with the number of electrons in the dot. The width of the barriers and the number of electrons in the dot are plotted for two different backgate voltages.

Fig. 4.5 shows the difference of how the barriers are controlled. The barrier under the

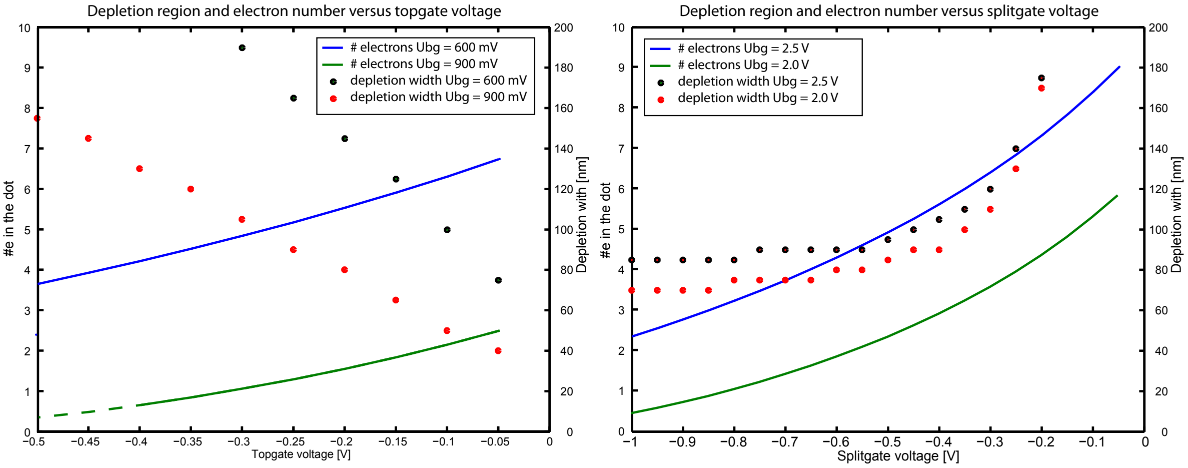

Figure 4.5: Number of electrons and depletion width versus gate voltage. The backgate is set to $V_{BG} = 600\,\mathrm{mV}$ and $V_{BG} = 900\,\mathrm{mV}$ for the topgate device (left) and $V_{BG} = 2.0\,\mathrm{V}$ and $V_{BG} = 2.5\,\mathrm{V}$ for the splitgate device (right). The number of electrons decreases for a higher (more negative) gate voltage. The depletion width is reduced for lower (less negative) topgate voltage, while it is increased for lower (less negative) splitgate voltage. For higher (more negative) splitgate voltage, the depletion width saturates. When the topgate voltage gets too high, a dot under the topgate is created (dashed line).

topgate gets larger for a more negative gate voltage, while a more negative voltage applied to the splitgates results in a smaller barrier. For topgates, the width depends linearly on the topgate voltage. However, the width also depends on the backgate voltage and the maximum width that can be obtained is different for different backgate voltage. The barriers in the splitgate device are less dependent on the backgate voltage. This is because the barriers are shifted in position when the backgate voltage is changed. For the splitgate device the width is limited by the p-n-junction, and therefore the barrier has a lower bound instead of an upper bound.

From the simulations we see that both the topgate device as the splitgate device are very suitable to create a dot with tunable barriers. However, there are some limitations. The voltage adjusted to the topgates must be adjusted to the backgate voltage to still get a dot in the nanotube. For a large backgate voltage, the nanotube is no longer depleted underneath the topgates. On the other hand, when the topgate voltage gets too high, a second, unwanted, p-type dot is created underneath the topgate. Within this region, the width of the depletion region depends linearly on the topgate voltage.

The transmission probability from the leads to the dot for electrons close to the Fermi energy can be calculated using the WKB approximation [47]. For the topgate device, the barriers can be made very transparent and the tunnel probability can be controlled from approximately unity to approximately zero. The p-n junctions in the splitgate device limit the barrier width and thus limit the transparency. Here, the barrier height is given by $E - U_b(x) = \min(|E - U_c(x)|, |E - U_v(x)|)$, where U_c and U_v are the energies of the conduction and valence band respectively. For the range of given voltages, the tunnel probability can be tuned from approximately zero to $T = 4 \cdot 10^{-5}$ using the splitgate. Assuming four-fold degeneracy, the resistance of such a barrier equals $R = 79\,\mathrm{M\Omega}$. Other simulations have

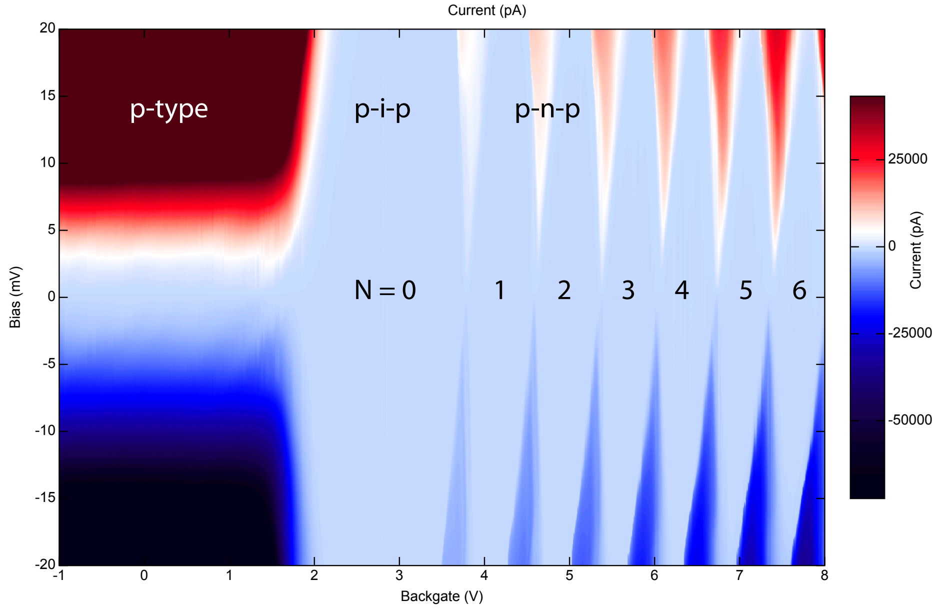

Figure 4.6: Recent experimental data for a suspended nanotube in a splitgate device. The polarity of the nanotube is changed from *p-p-p* to *p-i-p* to *p-n-p*. The measurement was done for $T = 2\,\mathrm{K}$.

shown that the tunnel probability can be increased to $T = 0.10$ by applying a voltage of $V_{SG} = -5.0\,\mathrm{V}$ to the splitgate.

Recent experiments have confirmed that it is possible to make a quantum dot by making a *p-n-p* junction in a carbon nanotube, see Fig. 4.6. The device used for this experiment is very similar to the one presented in this subsection. The measurements were done for a suspended nanotube, which has a bandgap of $E_g \approx 78\,\mathrm{meV}$. The splitgate voltages were kept constant at $V_{SG} = -50\,\mathrm{mV}$ and the backgate and source-drain bias were swept. The data shows that the nanotube is completely doped with holes for low backgate voltage, and that an n-type dot can be formed by increasing this voltage. The charging energy is approximately $E_C = 40.8\,\mathrm{meV}$ for the first electron and decreases when more electrons are added to the dot.

4.2.2 Level spacing in a quantum dot in a semiconducting nanotube

The Thomas-Fermi simulations, and recent experiments, show that both splitgates and topgates can be used to control a quantum dot in a semiconducting nanotube. Using the splitgate device, it is possible to suspend the nanotube which avoids the effect of trapped charges in the oxide layer, and increases the coupling to the SET. This is not possible for a topgate device. For this reason we will use a device with splitgates for the next simulations (Fig. 2.8).

We are interested in the level spacing of the electrons in the quantum dot and we will use the Hartree approximation for these calculations. For the simulation, we use the same device as in the previous subsection. For the Schrödinger equation we use an effective mass of $m^*/m_e = 0.03$ (corresponding to a gap of $E_g = 300\,\mathrm{meV}$). We fix the number of electrons and calculate the self-consistent solution as described in subsection 3.2.2. We take the energy of the highest occupied orbital compared to the chemical potential of the leads for different

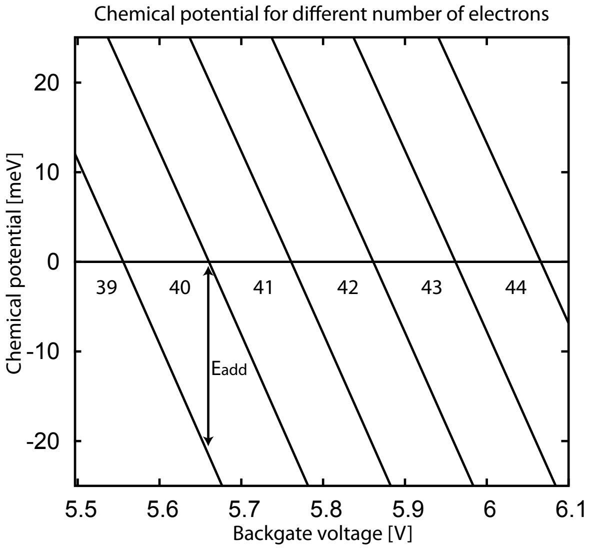

Figure 4.7: Chemical potential of the groundstate for 40 to 45 electrons. When the calculated lines cross with the chemical potential of the leads ($\mu = 0$), it is energetically more favorable to let an electron tunnel into the dot. When the 41st or 45th electron is added, the addition energy corresponds to the charging energy plus the level spacing.

gate voltages and different electron number. Fig. 4.7 gives the results for 40 to 45 electrons. In the simulations, every $4N + 1$ electron is put in a higher orbital, which correspond to the four-fold filling in the presence of valley-degeneracy.

When the self consistent solution is found, we look at the energy of the last electron added to the dot. Fig. 4.7 gives the energy of the highest occupied orbital versus gate voltage for different number of electrons. When the line of the calculated energies crosses the Fermi energy of the leads (which is set to $E_F = 0$), this corresponds to an electron entering the dot. From these calculations, relevant parameters of the quantum dot can be obtained. First of all, the capacitance of the backgate is given by the gate voltage difference between two electrons entering the dot. The capacitance of the backgate to the dot is $C^{BG}_{NT_{dot}} = 1\mathrm{e}/105\,\mathrm{mV} = 1.5\,\mathrm{aF}$.

For the backgate voltage corresponding to an electron entering the dot, the the energy difference between the energy of N and $N - 1$ electrons equals the addition energy. For the 41st and 45th electron, the addition energy equals the charging energy plus the level spacing, since for these cases the electrons have to occupy a higher orbital (using the four-fold filling). The addition energy for these two electrons is $E^{(41)}_{add} = 21.7\,\mathrm{meV}$ and $E^{(45)}_{add} = 21.3\,\mathrm{meV}$. For the other electrons the addition energy equals the charging energy: $E^{(42)}_{add} = 20.8\,\mathrm{meV}$, $E^{(43)}_{add} = 20.7\,\mathrm{meV}$ and $E^{(44)}_{add} = 20.6\,\mathrm{meV}$. From these results it follows that the level spacing is of the order of $\delta = 0.8\,\mathrm{meV}$. The charging energy decreases when the electron number is increased. Since the charging energy is inversely proportional to the self capacitance of the dot, this is what we expect. For a larger number of electrons, the dot gets larger and the self capacitance increases.

Next, we look at the spectrum of the electrons in the quantum dot for a fixed number of electrons. The gate voltages are tuned until the Thomas-Fermi approximation gives the desired number of electrons. The spectrum with corresponding wavefunctions are calculated

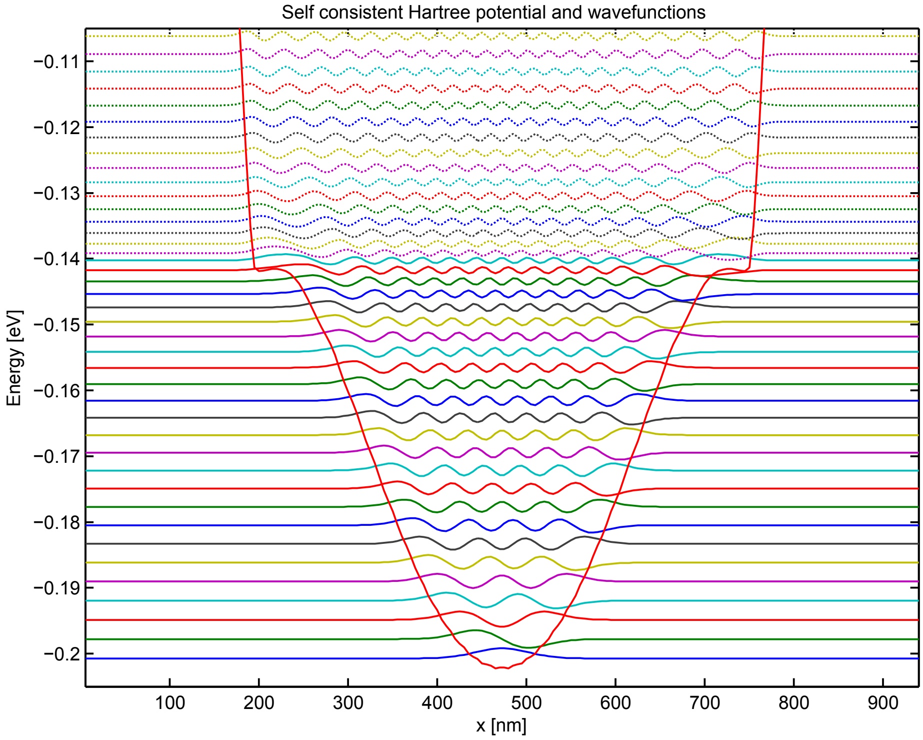

Figure 4.8: Self consistent potential and wavefunctions of the Hartree approximation for 100 electrons. The solid lines correspond to filled states, dashed lines correspond to empty states.

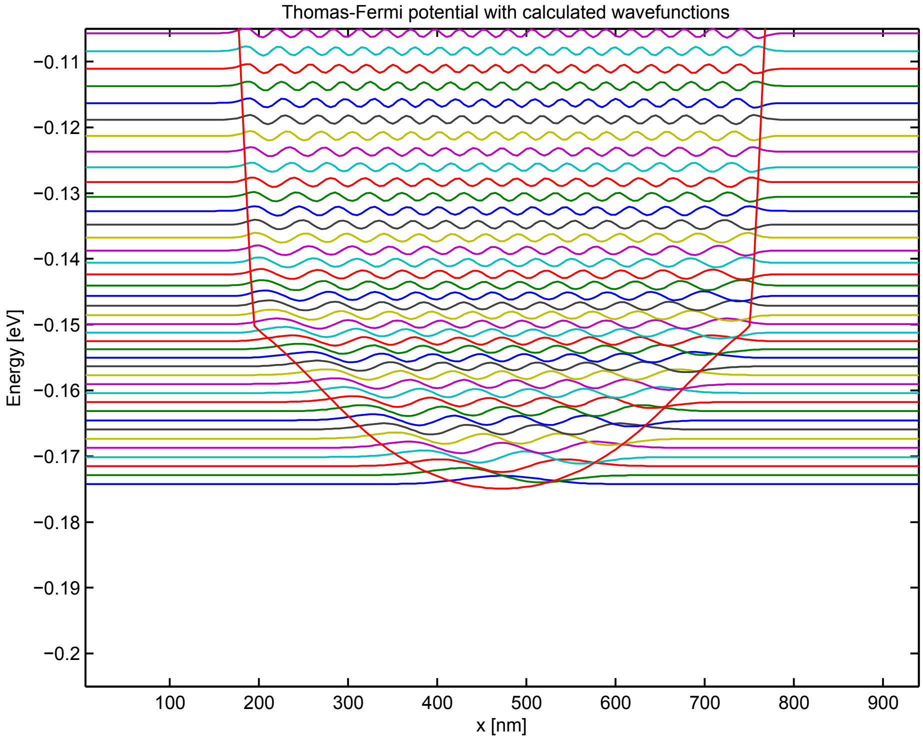

Figure 4.9: Thomas-Fermi potential for 100 electrons with calculated wavefunctions. The axis are equal to the axis in Fig. 4.8. The Fermi energy is $E_F = -E_g/2 = -0.15\,\text{eV}$.

for the found potential, which we will refer to as the Thomas-Fermi spectrum. We will not use the found wavefunctions for any further calculations.

From the initial guess given by the Thomas-Fermi approximation, we will continue and calculate the Hartree approximation. The Hartree approximation results in a self consistent potential with corresponding (self consistent) wavefunctions. The spectrum obtained from the Hartree approximation is compared with the spectrum calculated from the Thomas-Fermi potential. In Fig. 4.8, the self consistent Hartree potential and wavefunctions for a dot with 100 electrons are plotted. In Fig. 4.9, the Thomas-Fermi potential is given for the same dot and same number of electrons, together with the calculated wavefunctions and eigenvalues for this potential. The axis in both plots are equal such that a good comparison can be made between the two spectra.

The first thing to notice is the large difference in the potentials. The self consistent Hartree potential is much steeper than the Thomas-Fermi potential, resulting in a larger level spacing for the Hartree approximation. Also, near the Fermi energy, there is a bump in the Hartree potential at the edge of the dot. Here, the energies levels are closer to each other, compared to states with a lower energy. The bump in the potential is typical for the self consistent Hartree potentials we find.

In the Thomas-Fermi approximation, the Fermi energy is predefined and equals $E_F = -Eg/2 = -150\,\mathrm{meV}$. For the Hartree approximation, the Fermi energy is defined by the energy of the highest occupied orbital and equals $E_F = -140\,\mathrm{meV}$ for 100 electrons. For both spectra, the level spacing is larger for energies higher than the Fermi energy. For this regime, the Fermi energy lies inside the bandgap and so the nanotube is depleted. The potential is therefore very steep for energies higher than the Fermi energy corresponding to a larger level spacing.

The calculated potentials with corresponding spectra are different from any simple model potential, especially for the Hartree approximation. We take a closer look at the level spacings for the Thomas-Fermi potential and the Hartree approximation for 100 electrons and for 45 electrons. The calculated level spacings for 100 electrons and for 45 electrons are given in Fig. 4.10. Both the level spacing for the Thomas-Fermi spectrum as for the self consistent Hartree spectrum is given.

For low eigenvalue numbers, the Thomas-Fermi spectrum is relatively constant, corresponding to a harmonically shaped potential. For higher energies, the level spacing increases, suggesting that the hard wall nature of the potential becomes more important. The level spacing at high energy obtained from the Hartree approximation converges to the Thomas-Fermi spectrum, meaning that the hard wall like potential is approximately the same in both approximations. For energies lower than the Fermi-energy however, the level spacing is significantly larger for the Hartree approximation. The spacing between the highest occupied level and lowest unoccupied level is the smallest. Although we have used a continuum approximation instead of filling the actual orbitals, also for the Thomas-Fermi approximation, a minimum in the level spacing is observed.

When we compare the spectrum of the two different potentials (Fig. 4.8 and 4.9), we see that the number of states below the Fermi-energy is different for both cases. In the Hartree approximation, the Fermi-energy is defined by the energy of the highest occupied level, and therefore there are 25 levels below the Fermi-energy for 100 electrons. For the Thomas-Fermi approximation, there are only 18 states below the Fermi-level ($E_F = -E_g/2 = -0.15\,\mathrm{eV}$). Because the number of states below Fermi energy is different for both approximations, the minimum in the level spacing occurs for different eigenvalue numbers.

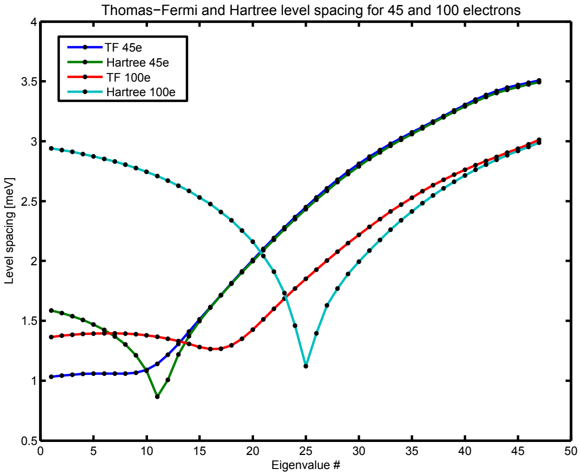

Figure 4.10: Level spacing for the Thomas-Fermi potential and the self consistent Hartree approximation for 45 and 100 electrons. The levelspacing for eigenvalue number 1 corresponds to the energy difference of the first and second state. For eigenvalue number 2 it is the energy difference of state 2 and 3, etcetera. A four fold filling is used, such that for 45 electrons the Hartree levels are filled up to the 11th level for 45 electrons and up to the 25th level for 100 electrons. The level splitting is smallest between the highest occupied state and lowest unoccupied state.

The solution of both approximations is the one of which the total energy, including the electrostatic energy of electrons interacting with charge on the gates, is minimal. This implies that the charge distribution in the dot will always converge to a smooth charge distribution which is not too different from the Thomas-Fermi approximation. We indeed observe that the charge distribution from the Hartree approximation and the Thomas-Fermi approximation is almost identical when the number of electrons is large. Consequently, the potential will be such that the corresponding charge distribution is as smooth as possible. From this point of view, we can conclude that the change in spectrum we observe is purely a electrostatically driven phenomena.

4.3 Quantum dots with two electrons

When treating a large number of electrons, both the Hartree approximation and Thomas-Fermi approximation are useful. The approximations can be used to calculate, among other things, depletion regions in a nanotube, the (self consistent) spectrum of a quantum dot and charging energies for different number of electrons. For a small number of electrons however, self interaction of the electrons results in large errors. We could avoid the self interaction by using a unrestricted form of the Hartree approximation, meaning that we have to solve a different Hartree equation for each electron. The problem with this unrestricted Hartree approximation is that it does not guarantee that the wavefunctions are orthogonal, as required by the Pauli principle. For two electrons with opposite spin, the spin parts of the wavefunctions are orthogonal and this method could be used. For the same argument, the method can be used for up to four electrons when valley degeneracy is present.

However, the Hartree approximation only includes Coulomb repulsion and completely neglect correlations between the electrons. To model the two electrons in the double dot, the Hartree approximation is therefore no longer sufficient and we therefore use the exact diagonalization calculations (section 3.3). For all calculations, we assume that the valley degeneracy is broken with a small magnetic field parallel to the nanotube. We ignore the Zeeman effect which simply shifts the energies of the triplet states T^+ and T^- by $\pm 58\,\mu\text{eV}\text{T}^{-1}$ [20].

4.3.1 Singlet-triplet splitting of two electrons in a double dot

The device we will use to make the double dot is a device with five splitgates. In the device, the nanotube is suspended such that effects from trapped charges in the oxide layer are avoided, and coupling to the SET is increased. We use five splitgates, from which the middle splitgate is used to split the dot into a double dot. The vertical separation between the splitgates and the nanotube is 100 nm. The width of the splitgates equals 100 nm and the distance in between the splitgates is also 100 nm. By varying the voltages of the five independent gates, it is expected that the double dot can be controlled. The backgate is not used in this setup (see also Fig. 2.9).

In the simulation, we keep the outer two splitgates fixed at a given voltage, which dope the nanotube with holes. The middle splitgate is also kept at a constant voltage. The other two splitgates are used to control the energy in each dot separately. We calculate the bare potential as described in subsection 3.3.3 for different gate voltages and solve the two-electron Schrödinger equation using the 2D screened Coulomb interaction 'potential' calculated for the device.

When there is one electron in each dot (the (1,1) situation), the singlet-triplet splitting is expected to be very small. For the (0,2) or (2,0) case, with one electron in each dot, we can estimate the singlet-triplet splitting using the shell filling model. The singlet-triplet splitting is given by the level spacing minus the exchange interaction $\Delta ST_{0,2} = \hbar\omega_0 - E_{xc}$. Here ω_0 is the trap frequency of the potential and E_{xc} is the exchange correlation energy difference due to the anti-symmetry requirement of the (total) wavefunction (E_{xc} is often referred to as J).

For GaAs 2DEG systems, the double dot experiment has been well characterized experimentally. For these systems, the level splitting $\hbar\omega_0$ is about 2 meV for a single dot. The exchange correlation interaction is typically half of the level spacing $E_{xc} = \hbar\omega_0/2 = 1\,\text{meV}$ such that the singlet-triplet splitting is $\Delta ST_{0,2} = \hbar\omega_0/2$. For nanotubes, the level spacing for many electrons is of the same order of magnitude. We therefore expect that singlet-triplet splitting is similar to that of GaAs systems.

Fig. 4.11 shows two calculated bare potentials for the double dot for the splitgate device with five splitgates for a nanotube with a bandgap of $E_g = 300\,\text{meV}$. The voltage at the outer two splitgates is set to $V_{SG_{Leads}} = -2.5\text{V}$ and the middle splitgate is kept fixed at $V_{SG_M} = +100\text{meV}$. In the left plot, the chemical potentials of the two dots are aligned such that there is one electron in each dot. The two splitgate voltages are $V_{SG_L} = V_{SG_R} = 1.350\text{V}$. Changing the voltages to $V_{SG_L} = 1.500\text{V}$ and $V_{SG_R} = 1.200\text{V}$ results in the right picture, where both electrons are in the left dot [1].

For both potentials we calculate the single particle level spacing $\hbar\omega_0$. For the (1,1) case, the level spacing is approximately zero, as expected, since the interdot coupling is small. The

---

[1] Note that we have ignored the valence band in the calculations of the potentials given in Fig. 4.11. When the barrier is too high, this could result in co-tunneling through the valence band. Ideally, the barrier height is (much) lower than $E_g/2$.

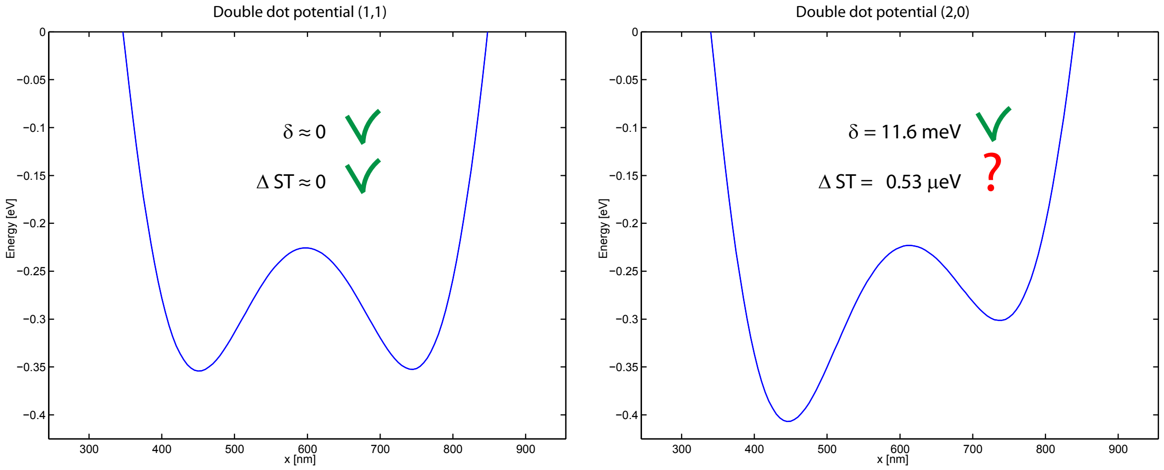

Figure 4.11: Double dot bare potential energy for the two electrons. The solid lines correspond to the single-electron energy levels calculated from the exact diagonalization with the screened Coulomb potential for the device. The dashed lines are the single-electron energies without Coulomb interaction (the difference equals the single particle level spacing). Left: the chemical potentials are aligned such that there is one electron in one dot. The calculated singlet-triplet splitting is $\Delta ST_{11} \approx 0$ (the calculated value is $3 \cdot 10^{-15}$ eV, which is of the same order as the truncation error). The two levels $S_{1,1}$ and $T_{1,1}$ are obviously not distinguishable in the plot. The single particle level spacing ($\hbar\omega_0$) for the given potential is $\delta_{11} \approx 0$ ($1 \cdot 10^{-14}$ eV). Right: the potential is tilted such that the two electrons are now both in the left dot. The single particle level spacing is $\delta_{20} = 11.6\,\text{meV}$. The calculated singlet and triplet energies are again not distinguishable. The singlet-triplet splitting for the (2,0) case is only $\Delta ST_{2,0} = 0.53\,\mu\text{eV}$.

singlet-triplet splitting $\Delta ST_{1,1}$ is of the same order as the single particle level spacing and is approximately zero. The (1,1) states are thus degenerate. In the real double dot experiment, the (1,1) singlet and triplet states can mix due to interaction with the environment because of this degeneracy.

For the (2,0) case for the given gate voltages, the single particle level spacing is $\delta = 11.6\,\text{meV}$, which is (very) large compared to the typical level splitting of GaAs. However, the singlet-triplet splitting for the (2,0) case is about four orders of magnitude smaller than expected: $\Delta ST_{2,0} = 0.53\,\mu\text{eV}$. The calculated 2D wavefunctions can be found in appendix A.

The small singlet-triplet splitting suggest that the exchange correlation energy E_{xc} is approximately equal to the level spacing $\hbar\omega_0$, or, that something else is going on. In the next subsection, we will use a simple model to understand why the singlet-triplet splitting is so much smaller than expected.

4.3.2 The harmonic oscillator model

The simplest model to verify the results of the simulations is the well known harmonic oscillator model. The external potential for the harmonic oscillator is given by

$$U_{ext}(x) = \frac{1}{2} m^* \omega_0^2 x^2 \tag{4.6}$$

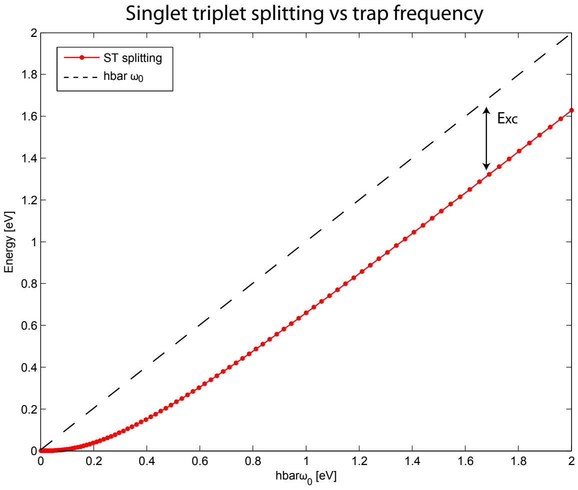

Figure 4.12: Singlet-triplets splitting versus trap frequency. The dashed black line corresponds to the level spacing $\hbar\omega_0$, which is the singlet-triplet splitting for non-interacting electrons. According to the shell filling model, the singlet-triplet splitting equals the single particle level splitting minus the exchange correlation energy E_{xc}.

where ω_0 is the trap frequency of the potential. We solve the two-electron Schrödinger equation for the harmonic oscillator potential. We use a cut-off distance of $\mu = 1\,\text{nm}$ and a relative dielectric constant $\epsilon_r = 1.0$ for the Coulomb interaction 'potential'. These parameters correspond to a nanotube which is suspended. For the calculations, we use the same effective mass as in the previous subsection ($m^* = 0.0293 m_e$, corresponding to a bandgap of $E_g = 300\,\text{meV}$).

According to the shell filling model, the singlet-triplet splitting is given by the level spacing minus the exchange correlation energy: $\Delta ST = \hbar\omega_0 - E_{xc}$. The singlet-triplet splitting for different trap frequency ω_0 is plotted in Fig. 4.12. For high trap frequencies, the singlet-triplet splitting is equal to the level splitting minus some constant energy, the exchange correlation interaction E_{xc}. For low trap frequencies, the singlet-triplet splitting goes to zero, suggesting that the exchange energy equals the single particle level spacing. A more thorough understanding can be gained by taking a closer look at the results.

By applying the Hamiltonian to the two-electron wavefunctions, we get the energies of the electrons:

$$\begin{gathered}\langle\Phi(x_1,x_2)|\hat{H}|\Phi(x_1,x_2)\rangle \\ = \\ \langle\Phi(x_1,x_2)|\frac{\hbar^2}{2m^*}(\frac{d^2}{dx_1^2}+\frac{d^2}{dx_2^2})+U_{ext}(x_1)+U_{ext}(x_2)+V_C(x_1,x_2)|\Phi(x_1,x_2)\rangle \\ = \\ E_k+E_{pot}+E_C\end{gathered} \tag{4.7}$$

The Coulomb interaction energy is thus found by the overlap of the wavefunction with the 2D Coulomb interaction 'potential'. The symmetric wavefunction is in general maximal at $x_1 = x_2$, where the Coulomb interaction potential is maximal. The anti-symmetric wavefunction has a node at $x_1 = x_2$, such that the overlap is much smaller compared to the symmetric

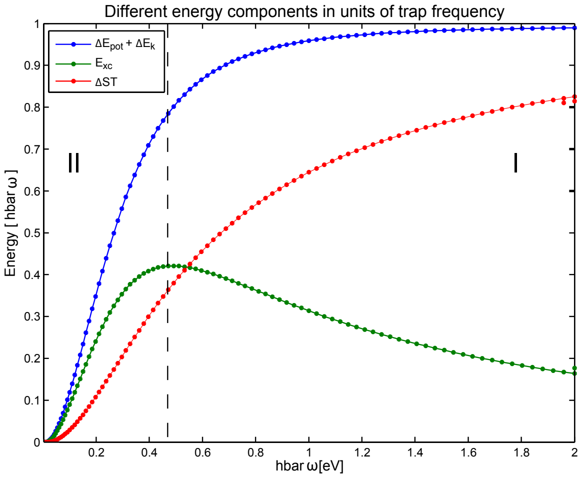

Figure 4.13: Different energy components divided by the level spacing $\hbar\omega_0$. For a very high trap frequency, the single particle level spacing equals $\Delta E_k + \Delta E_{pot} = \hbar\omega_0$ and the singlet-triplet splitting equals $\hbar\omega_0 - E_{xc}$. When the trap frequency is lowered, the exchange correlation energy increases (I). For region II, the exchange correlation energy starts to decrease again. Also, ΔE_k and ΔE_{pot} decrease.

wavefunction. This difference in energy due to the different Coulomb interaction is know as the exchange correlation energy E_{xc}.

The singlet-triplet splitting is thus given by

$$\begin{aligned}\Delta ST &= (E_{k_{triplet}} - E_{k_{singlet}}) + (E_{pot_{triplet}} - E_{pot_{singlet}}) + (E_{C_{triplet}} - E_{C_{singlet}}) \\ &= \Delta E_k + \Delta E_{pot} - E_{xc}\end{aligned} \tag{4.8}$$

which is consistent with the shell filling model when $\Delta E_k + \Delta E_{pot} = \hbar\omega_0$.

In Fig. 4.13, the different energy components, relative to the level spacing, are plotted. For very high frequency (indicated by I), the difference in kinetic energy and potential energy between the triplet and singlet states converges to $\Delta E_k + \Delta E_{pot} = \hbar\omega_0$. Here, the singlet-triplet splitting is consistent with the shell filling model, since $\Delta ST = \hbar\omega_0 - E_{xc}$ holds. When the trap frequency gets lower, the exchange correlation energy E_{xc} increases. This can be explained from the shape of the wavefunctions. For lower trap frequency, the wavefunctions get broader, and the difference in overlap with the Coulomb interaction potential increases. However, for a trap frequency lower than approximately $\hbar\omega_0 = 400\,\mathrm{meV}$ (II in Fig. 4.13), the exchange correlation energy decreases again. At the same time, ΔE_k and ΔE_{pot} decrease. This means that the singlet-triplet splitting for a low trap frequency is small because of the small difference in the kinetic and potential energy, and not because of a large exchange correlation energy. For this region, the shell filling model is no longer valid.

Fig. 4.14 shows the 2D wavefunctions of the singlet and triplet state and the corresponding charge distribution. In (a), the trap frequency is very high and the wavefunctions and charge distribution are as expected from the shell filling model. The charge distribution is approximately 10 nm broad. For lower trap frequency (b), the 2D singlet wavefunction gets a local minimum at $x_1 = x_2$, which reduces the Coulomb energy. Here, the charge distribution is about 15 nm broad and gets a local minimum in the middle. The charge distribution is further broadened for a trap frequency of $\hbar\omega_0 = 20\,\mathrm{meV}$. The singlet 2D wavefunction is now

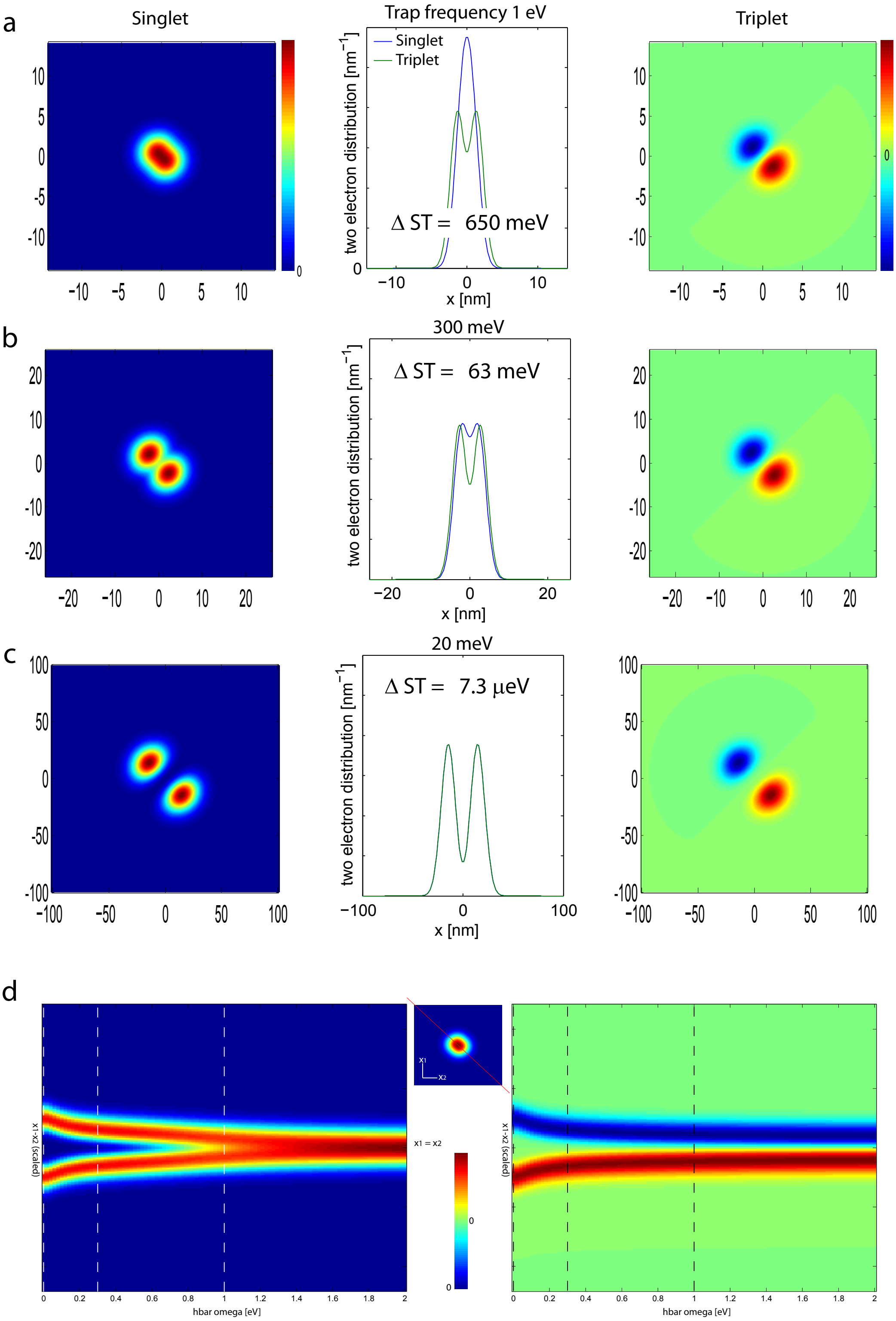

Figure 4.14: 2D wavefunctions of the singlet and triplet with corresponding charge distribution for different trap frequencies (a,b,c). For very high trap frequency (a), the 2D wavefunctions and corresponding charge distribution is like expected from the shell filling model. For lower trap frequency, the singlet gets a local minimum at $x_1 = x_2$ and at c, the charge distribution for the singlet is equal to that of the triplet. d: Linecut of the 2D wavefunction perpendicular to the line $x_1 = x_2$ for the singlet (left) and triplet (right) state. The vertical axis corresponds to $x_1 - x_2$, scaled to $\sqrt{\omega_0}$. The singlet wavefunction gets two maxima instead of one and for low frequency, the wavefunction is zero at $x_1 = x_2$. The triplet state only changes for relatively low frequency.

approximately zero at $x_1 = x_2$, such that the singlet and triplet wavefunction are (almost) equal, except for a phase difference. This results in a very low exchange correlation energy. Furthermore, since the shape of the wavefunctions is (almost) equal except for the phase difference, the kinetic and potential energy are also (almost) the equal. For this reason, the singlet-triplet splitting is very small.

Fig. 4.14.d. shows the linecut perpendicular to the line $x_1 = x_2$, representing the amplitude of the wavefunction for $x_1 - x_2$. The Coulomb energy is found by the overlap of the wavefunctions with the Coulomb interaction potential. At $x_1 = x_2$, the Coulomb interaction potential is maximal. When the trap frequency is lowered, the amplitude of the singlet wavefunction at $x_1 = x_2$ decreases. This results in a lower Coulomb interaction energy of the singlet state, such that the exchange correlation energy E_{xc} decreases. Eventually, for low trap frequency, the linecut of the singlet and triplet state are identical, except for the phase difference. At this trap frequency, the electrons have separated to save Coulomb energy, forming what one might call a Wigner crystal [48, 49]. Here, the spatial wavefunctions are equal except for the phase difference, such that the singlet-triplet splitting vanishes.

For the potential given in the previous subsection, the trap frequency of the (2,0) potential is $\hbar\omega_0 = 11.6\,\mathrm{meV}$. This trap frequency is high compared to a typical GaAs system. However, from the harmonic oscillator model we can conclude that for a potential with this trap frequency, the electrons are separated, resulting in the low singlet-triplet splitting found.

While this result may seem surprising, the difference from GaAs system can be understood from comparison of the relevant parameters. A typical dotsize in a nanotube is about 200 nm wide, which is much larger compared to the typical dotsize in GaAs systems ($d = 20\,\mathrm{nm}$ for $\hbar\omega_0 = 1\,\mathrm{meV}$). Moreover, the dielectric constant of the surrounding material equals one for a suspended nanotube, while it is more than ten times higher for GaAs ($\epsilon_{r_{GaAs}} = 13.8$). This, and the strong Coulomb interaction and correlation between the electrons due to the 1D nature of the nanotube, makes it energetically more favorable for the electrons to separate.

4.3.3 Controlling the double dot

For the double dot experiment, it is required that the interdot coupling (t_{12}) is much smaller than the singlet-triplet splitting. Due to the separation of the electrons however, the singlet-triplet splitting is very small. To meet the requirements of the double dot experiment, the interdot coupling must be decreased, or the confinement of the potential must be increased.

The design of the splitgate device is such that the energy of each dot, as well as the barrier in between them, can be controlled. Increasing the barrier results in a lower inter dot coupling. However, the barrier must be lower than half the bandgap, to suppress co-tunneling through the valence band. On the other hand, increasing the barrier results in a steeper potential and thus the energy cost for the occupation of the triplet state is increased.

From the this restriction, it would seem that having a large bandgap is favorable, such that a steep potential as well as a low interdot coupling can be realized. However, the effective mass is inversely proportional to the bandgap. Simulations have shown that having a tube with large bandgap results in a lower singlet-triplet splitting, even though the potential can be made much steeper.

As in real life, tuning the double dot until the right parameter space is found can take a long time. Fig. 4.15 show the final results. The energy diagram is calculated for a realistic device with five splitgates and a suspended nanotube. The outer two splitgates are set to $V_{SG1} = V_{SG5} = -50.0\,\mathrm{V}$ to create a steep confinement potential. The middle splitgate is kept at a fixed voltage, ranging from $V_{SG3} = +2.65\,\mathrm{V}$ to $V_{SG3} = +2.50\,\mathrm{V}$ The other two splitgates (SG_2 and SG_4) are adjusted such that the energy of the double dot allows only two electrons in the dot. The bare potential is calculated for the given gate voltages, and the two-electron Schrödinger equation is solved using the screened Coulomb interaction calculated for the device. By applying different gate voltages to SG_2 and SG_4, the potential is tilted until the anti-crossings of the singlet and triplet states are found.

The barrier height varies from $E_{barrier} = 87\,\mathrm{meV}$ for $V_{SG3} = +2.65\,\mathrm{V}$ to $E_{barrier} = 116\,\mathrm{meV}$ for $V_{SG3} = +2.50\,\mathrm{V}$. The corresponding calculated interdot couplings vary from $t_{12} = 2.33\,\mu\mathrm{eV}$ to $t_{12} = 0.9\,\mathrm{neV}$. When the barrier is lowered, the potential is more shallow and therefore the singlet-triplet splitting is decreased. For a relatively low barrier ($V_{SG3} = +2.65\,\mathrm{V}$), the singlet-triplet splitting is $\Delta ST_{2,0} = 0.72\,\mu\mathrm{eV}$, which is much smaller than the interdot coupling. For the high barrier ($V_{SG3} = +2.50\,\mathrm{V}$), the singlet-triplet splitting is still small: $\Delta ST_{2,0} = 2.11\,\mu\mathrm{eV}$, but it is much larger than the interdot coupling.

The simulations have shown that both the interdot coupling as the singlet-triplet splitting is changed by applying a different voltage to the middle splitgate. The singlet-triplet splitting remains small, even for very high gate voltage applied to the outer two splitgates. Experimentally, this means that the small singlet-triplet splitting of $\Delta ST = 2.11\,\mu\mathrm{eV}$ limits the temperature to $T \approx 25\,\mathrm{mK}$, to be able to initialize the system to the $S_{1,1}$ state.

When the gates are used to let the system go through the anti-crossing, the timescale of this operation is limited by the interdot coupling. Analogue to Eq.(2.25), the timescale corresponding to the interdot coupling of $t_{12} = 0.9\,\mathrm{neV}$ equals $t = 0.7\,\mu\mathrm{s}$. This means that if the time is shorter than this limit, the electrons will remain in the S_{11} state.

For a temperature much lower than $T = 25\,\mathrm{mK}$ and a timescale much longer than $t = 0.7\,\mu\mathrm{s}$, the spin states can be resolved by detecting the change of charge distribution, shown in Fig. 4.16.

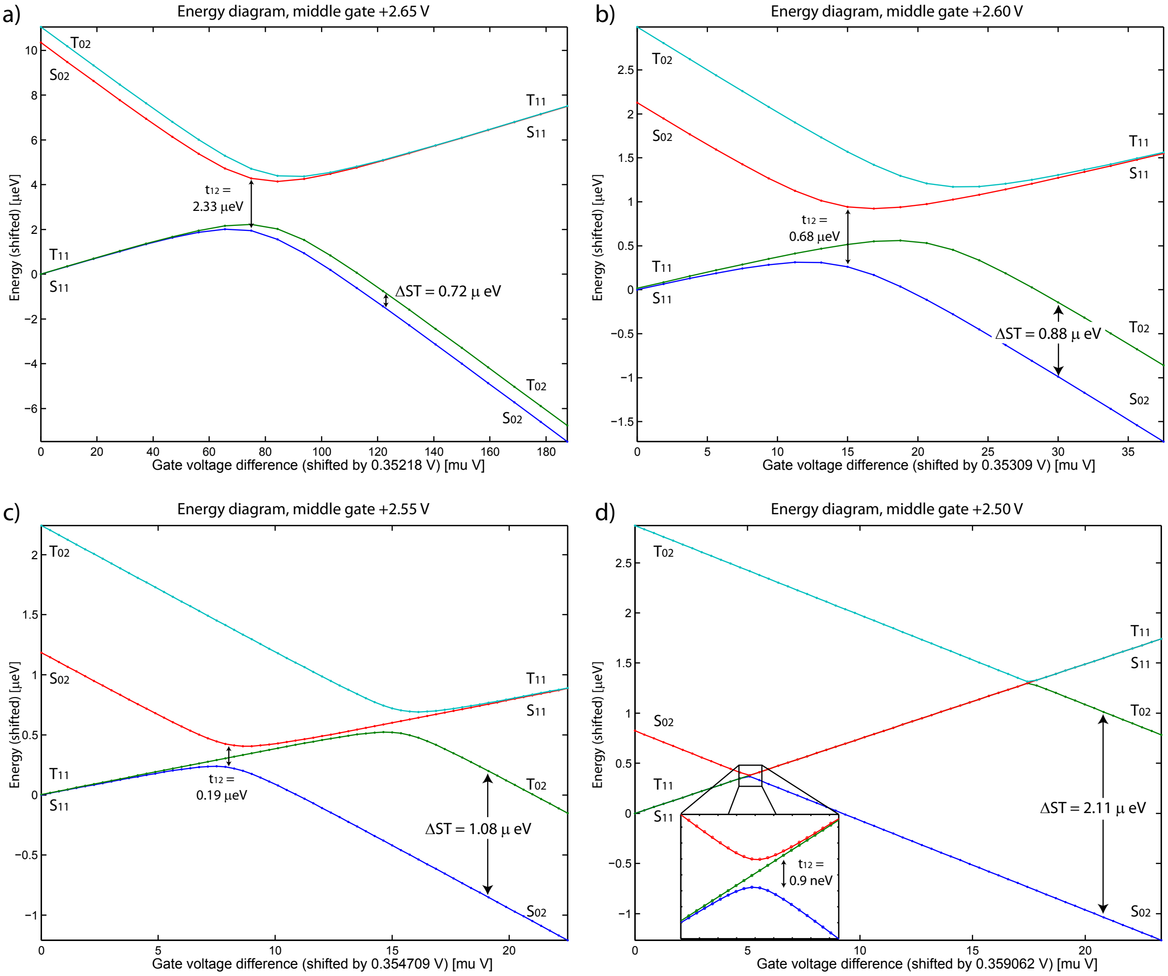

Figure 4.15: Calculated energy diagrams for different gate voltages of a realistic device with five splitgates. The interdot coupling and singlet-triplet splitting are dependent on voltage applied to the middle gate. The interdot coupling can be tuned such that it is much smaller than the singlet-triplet splitting, $t_{12} \ll \Delta ST$ (d). When the interdot coupling is decreased, the confinement potential is steeper, resulting in a higher singlet-triplet splitting.

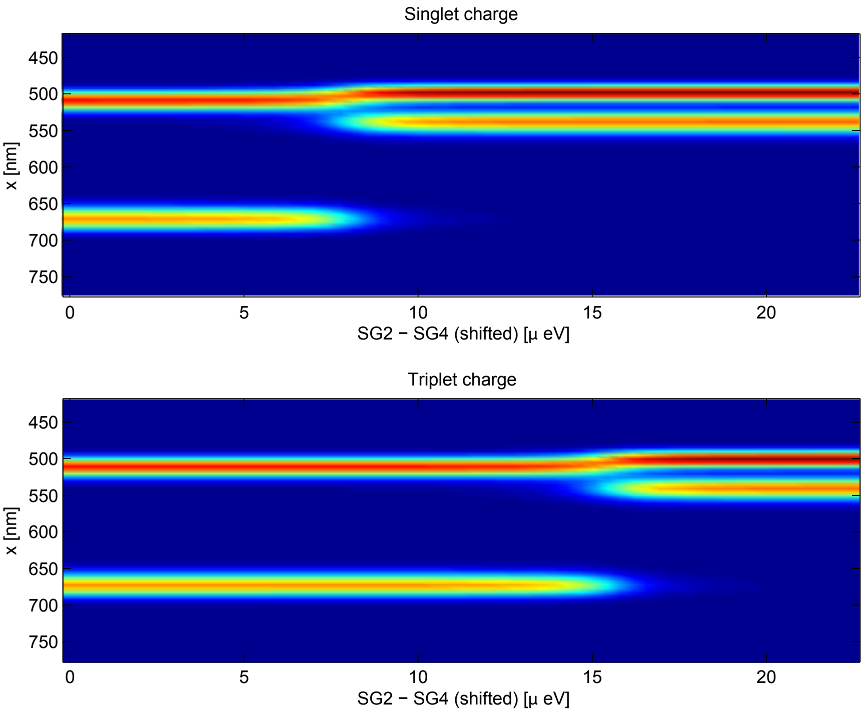

Figure 4.16: Charge distribution corresponding to the two lowest eigenstates in Fig. 4.15.c versus gate voltage. Starting on the left, both the singlet and triplet state is distributed over two dots. The left dot contains more charge compared to the right dot, indicating mixing of the (1,1) and (2,0) states. At about $SG_2 - SG_4 = 7\,\mu\mathrm{V}$ plus some offset, the singlet (1,1) and singlet (2,0) strongly mix. For higher gate voltage difference, the lowest state corresponds to the $S_{2,0}$ state. For the triplet state, the process is similar. The $T_{1,1}$ and $T_{2,0}$ states mix, and for high gate voltage difference, the first excited state equals the $T_{2,0}$ state. Since the transition of the ground state from $S_{1,1}$ to $S_{2,0}$ occurs at different gate voltages than for the triplet states, the spin state of the electrons can be resolved from the charge distribution.

Chapter 5

Conclusions and recommendations

5.1 Conclusions

Based on the results of 3D electrostatic simulations, where Poisson's equation is solved numerically, the conclusions are:

- Suspending a carbon nanotube results in a better coupling of the quantum dot to the single electron transistor (SET).
- Back-action from the SET to the quantum dot is reduced, when the nanotube is suspended.
- Suspending results in a better overall sensitivity of the SET.

Based on the results of 3D electrostatic simulations, combined with a Thomas-Fermi approximation and/or Hartree approximation for the carbon nanotube, the conclusions are:

- Both a device with topgates and a device with splitgates can be used to control a quantum dot in a semiconducting carbon nanotube. Splitgates can be used to form barriers by *p*-*n* junctions at the nanotube. Although the barriers formed by *p*-*n* junction are typically less transparent than barriers formed by locally depleting the nanotube, barriers formed by the *p*-*n* junctions are tunable from $T \approx 0$ to $T = 0.10$ or higher. Recent experiments have shown that it is possible to make a quantum dot by making a *p*-*n*-*p* junction in a suspended nanotube, using splitgates.
- The charging energy for a single dot containing about 40 electrons in a carbon nanotube device with splitgates is of the order of 20 meV and decreases when the number of electrons is increased. The levelspacing for this dot is $\delta = 0.8\,\mathrm{meV}$ and increases with the number of electrons.
- The spectrum of the quantum dot, obtained from the Hartree approximation, will be such that the corresponding charge distribution is as smooth as possible. For this spectrum, the level splitting is highest for the lowest eigenstates, and smallest between the highest occupied state and lowest unoccupied state. The spectrum corresponding with the Thomas-Fermi potential is also highest for the lowest eigenstates, and is also the smallest at the Fermi-energy. The Fermi-energy defined for the Thomas-Fermi approximation is lower then the Fermi-energy obtained from the Hartree-approximation.

The charge distribution from the Hartree approximation and from the Thomas-Fermi approximation are almost identical.

Based on 3D electrostatic simulations with the Thomas-Fermi approximation for the leads of the nanotube only, combined with the exact diagonalization of the two-electron Schrödinger equation for the electrons in the dot, the conclusions are:

- A device with five splitgates can be used to tune a double dot in a suspended semiconducting carbon nanotube such that the electrons are in the (1,1) state, or in the (0,2) state.
- Singlet-triplet splitting in a single dot in a carbon nanotube is about four orders of magnitude smaller then the single particle level spacing $\hbar\omega_0$.
- The harmonic oscillator model has shown that the electrons will separate in order to save Coulomb energy for a realistic potential in a 1D nanotube. The electrons form what one might call a Wigner crystal. The shell filling model no longer applies in this regime.
- The double dot can be tuned such that the inter dot coupling is much smaller then the singlet-triplet splitting. A steeper potential results in a higher singlet-triplet splitting and a smaller interdot coupling. The height of the barriers is limited by the bandgap. Experimentally, the limit is set by the temperature $T \sim 25\,\mathrm{mK}$ and the time of the (1,1) to (0,2) transition $t \sim 0.7\,\mu\mathrm{s}$.

5.2 Recommendations

Regarding the code as developed, it is recommended to improve the user friendliness of the simulation program. Although the main focus of this project has been on realistic carbon nanotube devices, the code is also suitable for simple modeling of nanowire and 2DEG devices using the Thomas-Fermi approximation[1]. This gives the code great potential to be used as a simple program where a gate geometry and relevant parameters are given as input, and electrostatic potential and electric field lines, charge distribution and capacitances are output, such that the program can be used as a support in designing new devices.

In terms of the continuation of this project, one interesting subject that is recommended for further research is the few electron regime. In this thesis, only results of exact diagonalization for two electrons are presented. The Thomas-Fermi and Hartree approximations only make sense for many electrons. Using exact diagonalization in a point basis, the exact solution of the Schrödinger equation for maximal three electrons can be calculated on a modern personal computer using a reasonable number of grid points. The reason for this maximum is the scaling of the Hamiltonian which has dimensions $L^N \times L^N$, where L is the number of grid points, and N the number of electrons. A good and often used approximation to solve the many body Schrödinger equation for this regime is the configuration interaction method. In this approach, the Hamiltonian is written in a basis set of the Slater-determinants of cleverly chosen basis functions [41]. It will be interesting to have a closer look at the charge distribution for different number of electrons, and especially to find the electron number

---

[1] For detailed simulations of 2DEG and nanowire systems, a well developed program already exist [39,50,51], and further improvement of the developed code on these subjects is therefore not recommended

where the formation of a Wigner crystal occurs. One could think of performing the double dot experiment with two electrons, while many underlying states are also filled. Configuration interaction then covers the interaction between all electrons.

The developed code covers many relevant physics, but still more could be implemented. Although the pre-factor of the spin orbit coupling is small, spin-orbit coupling can still be strong due to the curvature of the nanotube [9, 52]. Another phenomena which we neglected in this work is inter-valley mixing and inter-valley scattering. We assume that the degeneracy is broken by a small magnetic field. Although full 3D self-consistent simulations are not per se suitable to study these phenomena itself, the effects could also be included in the program.

Furthermore, we have assumed that the dielectric constant of the nanotube equals unity. However, the polarizability is strongly dependent on the electronic structure of the nanotube and does not equal one [53, 54]. How the 1D dielectric behavior should be modeled properly in a 3D environment is at this point not clear. It does, however, mean that the Coulomb interaction in the nanotube is smaller than assumed, resulting in a higher singlet-triplet splitting.

Finally, from an experimental point of view, it is recommended to design a device where the splitgates are close to each other. The splitgates used for the results of section 4.3 are 100 nm wide and separated by 100 nm. By decreasing the separation between the splitgates a steeper potential can be realized, increasing the singlet-triplet splitting. However, the interdot coupling is also increased and thus the barrier in between the two dots should be higher for this case.

Appendix A

Double dot potential and wavefunctions

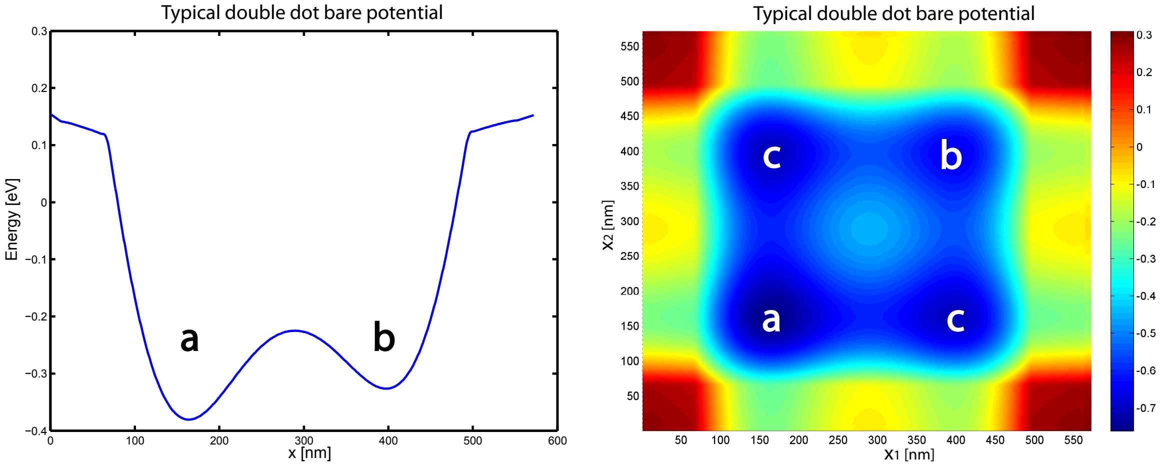

Figure A.1: Typical double dot potential. The cut of the 3D electrostatic potential along the nanotube gives the 1D confinement potential (left). Two electrons in the double dot see a 2D confinement potential (right). (a) corresponds to the left dot and (b) to the right. (c) (right only), corresponds to a superposition of the left and right dot.

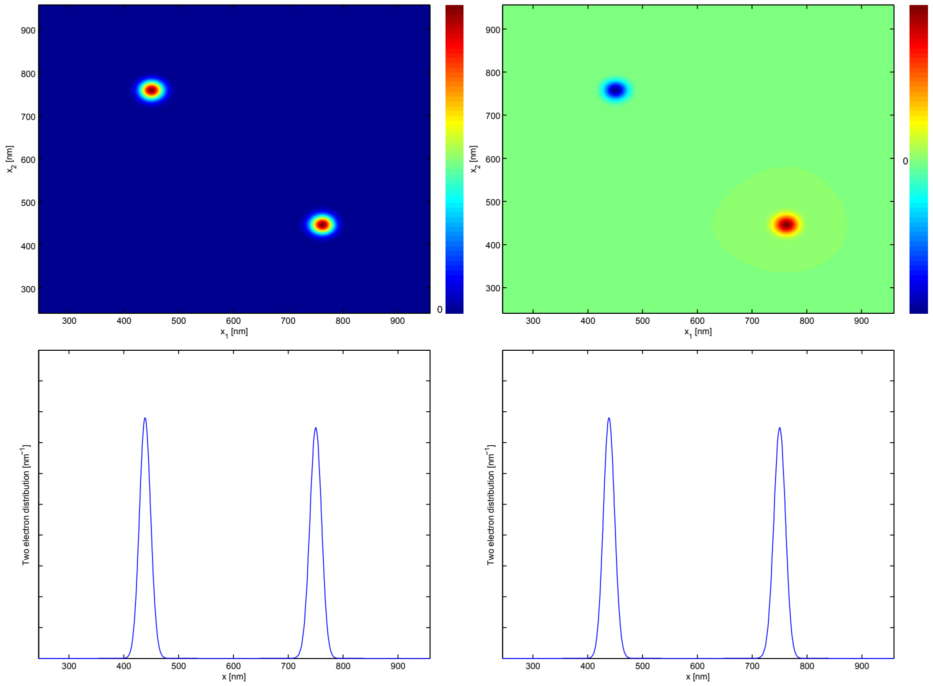

Figure A.2: Left: the S_{11} two-electron 2D wavefunction with corresponding charge distribution. Right: the same for the T_{11} state. The charge distribution is equal for both states. The spatial wavefunctions are equal except for a phase difference.

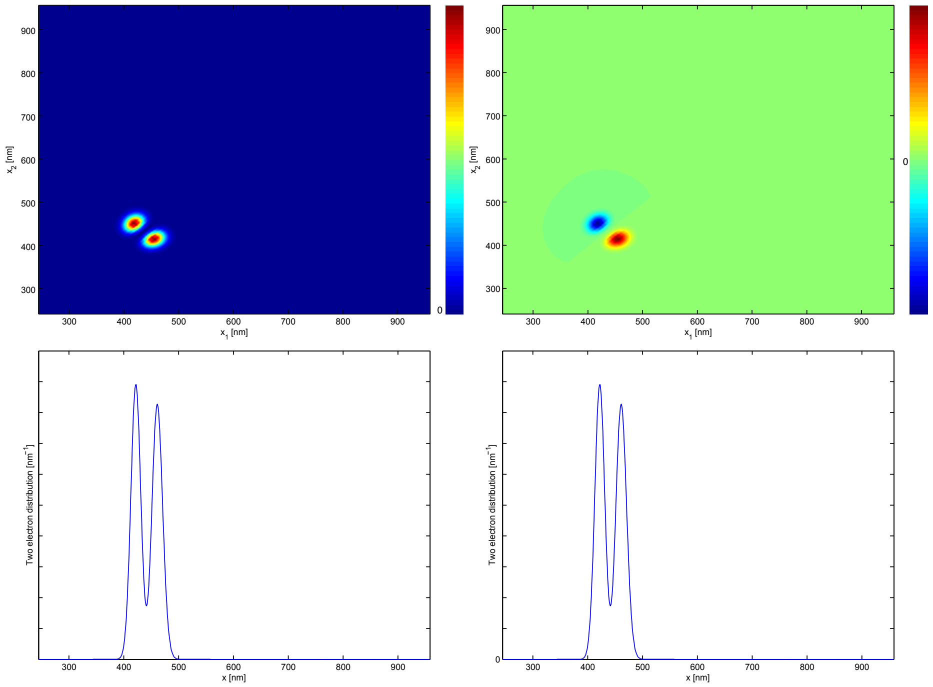

Figure A.3: The S_{20} (left) and T_{20} (right) two-electron 2D wavefunction and charge distribution. The singlet has a local minimum at $x_1 = x_2$, resulting in a very low energy difference between the singlet and triplet state.

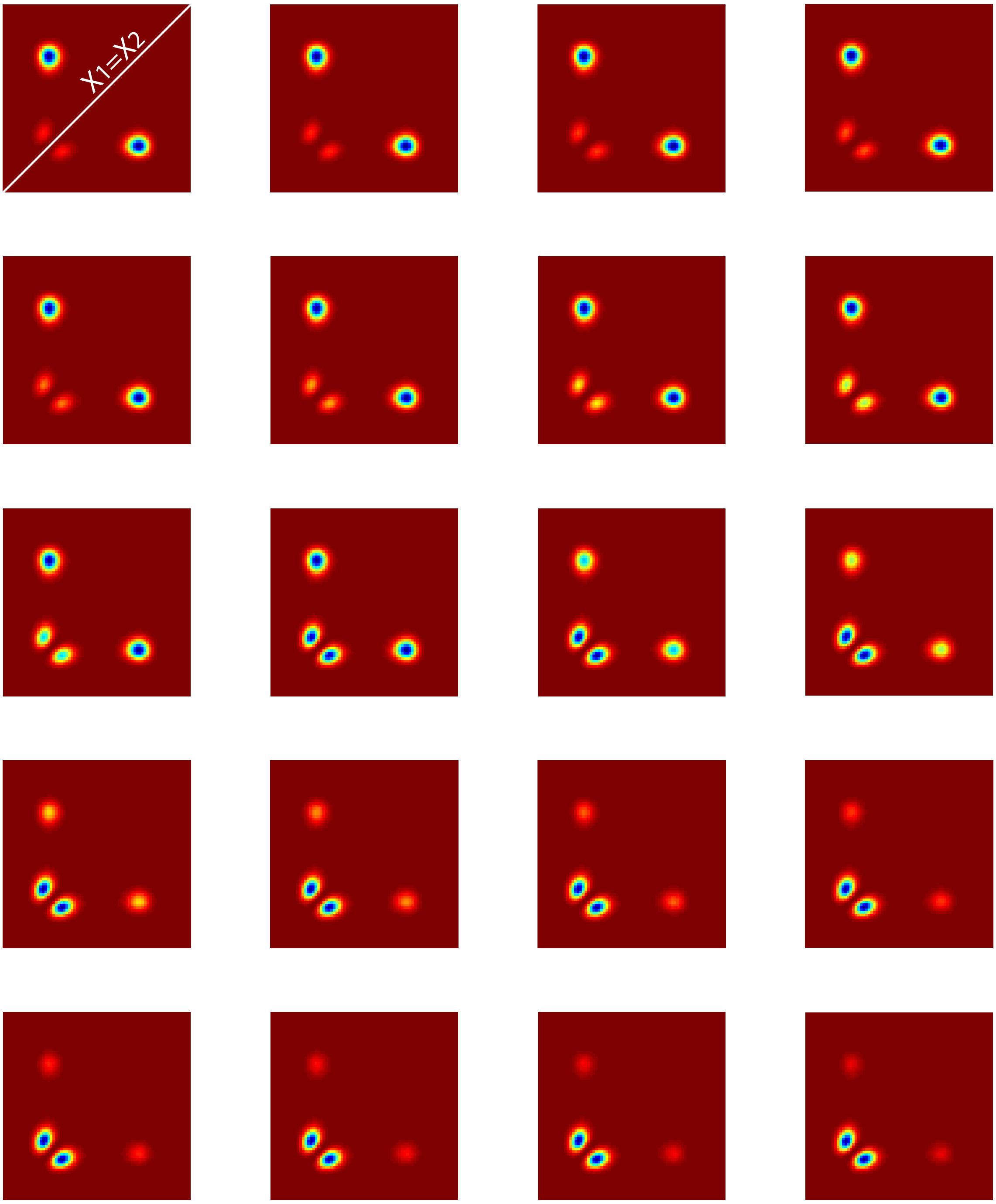

Figure A.4: Mixing of the S_{11} state with the S_{20} state, calculated for the double dot with parameters corresponding to the energy diagram from Fig. 4.15.c. The potential is tilted resulting in the transition from S_{11} to S_{20}.

Bibliography

[1] P. W. Shor, *Polynomial-time algorithms for prime factorization and discrete logarithms on a quantum computer*, Siam J.Sci.Statist.Comput., 26 (1997), p. 1484.

[2] D. DiVincenzo, *The Physical Implementation of Quantum Computation*, Scalable Quantum Computers: Paving the Way to Realization, (2001).

[3] D. Loss and D. P. DiVincenzo, *Quantum computation with quantum dots*, Phys. Rev. A, 57 (1998), pp. 120–126.

[4] F. H. L. Koppens, C. Buizert, K. J. Tielrooij, I. T. Vink, K. C. Nowack, T. Meunier, L. P. Kouwenhoven, and L. M. K. Vandersypen, *Driven coherent oscillations of a single electron spin in a quantum dot*, Nature, 442 (2006), p. 766.

[5] J. R. Petta, A. C. Johnson, J. M. Taylor, E. A. Laird, A. Yacoby, M. D. Lukin, C. M. Marcus, M. P. Hanson, and A. C. Gossard, *Coherent Manipulation of Coupled Electron Spins in Semiconductor Quantum Dots*, Science, 309 (2005), pp. 2180–2184.

[6] F. H. L. Koppens, J. A. Folk, J. M. Elzerman, R. Hanson, L. H. W. van Beveren, I. T. Vink, H. P. Tranitz, W. Wegscheider, L. P. Kouwenhoven, and L. M. K. Vandersypen, *Control and detection of singlet-triplet mixing in a random nuclear field*, Science, 309 (2005), p. 1346.

[7] S. Amasha, K. MacLean, I. P. Radu, D. M. Zumbuhl, M. A. Kastner, M. P. Hanson, and A. C. Gossard, *Spin-Dependent Tunneling of Single Electrons into an Empty Quantum Dot*, ArXiv e-prints, 709 (2007).

[8] S. Iijima, *Helical microtubules of graphitic carbon*, Nature, 354 (1991), pp. 56–58.

[9] D. Bulaev, B. Trauzettel, and D. Loss, *Spin-orbit interaction and anomalous spin relaxation in carbon nanotube quantum dots*, arXiv:0712.3767, (2007).

[10] P. Jarillo-Herrero, S. Sapmaz, C. Dekker, L. P. Kouwenhoven, and H. S. J. van der Zant, *Electron-hole symmetry in a semiconducting carbon nanotube quantum dot*, Nature, 429 (2004), p. 389.

[11] L. X. Benedict, S. G. Louie, and M. L. Cohen, *Static polarizabilities of single-wall carbon nanotubes*, Science, 275 (1997), pp. 1922–1925.

[12] P. Jarillo-Herrero, J. Kong, H. Van Der Zant, C. Dekker, L. Kouwenhoven, and S. De Franceschi, *Orbital Kondo effect in carbon nanotubes*, Nature, 434 (2005), pp. 484–488.

[13] N. Mason, M. Biercuk, and C. Marcus, *Local Gate Control of a Carbon Nanotube Double Quantum Dot*, Science, 303 (2004), pp. 655–658.

[14] S. Tans, M. Devoret, H. Dai, A. Thess, R. Smalley, L. Geerligs, and C. Dekker, *Individual single-wall carbon nanotubes as quantum wires*, Nature, 386 (1997), pp. 474–477.

[15] J. Kong, H. Soh, A. Cassell, C. Quate, and H. Dai, *Synthesis of individual single-walled carbon nanotubes on patterned silicon wafers*, Nature, 395 (1998), pp. 878–881.

[16] S. Iijima and T. Ichihashi, *Single-shell carbon nanotubes of 1-nm diameter*, Nature 363, 603 (1993), p. 605.

[17] J. Cao, Q. Wang, and H. Dai, *Electron transport in very clean, as-grown suspended carbon nanotubes*, Nat. Mat., 4 (2005), pp. 745–749.

[18] J. Cao, Q. Wang, M. Rolandi, and H. Dai, *Aharonov-Bohm Interference and Beating in Single-Walled Carbon-Nanotube Interferometers*, Phys. Rev. Lett., volume=93, number=21, pages=216803, year=2004, publisher=APS.

[19] S. Tans, M. Devoret, R. Groeneveld, and C. Dekker, *Electron±electron correlations in carbon nanotubes*, Nature, 394 (1998), p. 761.

[20] P. Jarillo-Herrero, J. Kong, H. S. J. van der Zant, C. Dekker, L. P. Kouwenhoven, and S. D. Franceschi, *Electronic transport spectroscopy of carbon nanotubes in a magnetic field*, Phys. Rev. Lett., 94 (2005), p. 156802.

[21] J.-C. Charlier, X. Blase, and S. Roche, *Electronic and transport properties of nanotubes*, Rev. Mod. Phys., 79 (2007), pp. 677–732.

[22] H. Ajiki and T. Ando, *Electronic states of carbon nanotubes*, J. Phys. Soc. Jpn., 62 (1992), pp. 1255–1266.

[23] P. R. Wallace, *The band theory of graphite*, Phys. Rev., 71 (1947), pp. 622–634.

[24] S. Sapmaz, *Carbon Nanotube Quantum Dots*, PhD thesis, TU Delft, 2006.

[25] E. Minot, *Tuning the band structure of Carbon Nantobes*, PhD thesis, Cornell University, 2004.

[26] G. Steele, *Nanotube calculations*, February 2007. http://kavli.nano.tudelft.nl/~gsteele/nanotubes/nanotube_calculations.pdf.

[27] R. Hanson, L. P. Kouwenhoven, J. R. Petta, S. Tarucha, and L. M. K. Vandersypen, *Spins in few-electron quantum dots*, Rev. Mod. Phys., 79 (2007).

[28] K. Ono, D. Austing, Y. Tokura, and S. Tarucha, *Current Rectification by Pauli Exclusion in a Weakly Coupled Double Quantum Dot System*, Science, 297 (2002), pp. 1313–1317.

[29] D. Martinez-Negrete Gasque, *A charge detector based on carbon nanotube quantum dots*, master's thesis, TU Delft, 2007.

[30] S. Heinze, J. Tersoff, R. Martel, V. Derycke, J. Appenzeller, and P. Avouris, *Carbon nanotubes as schottky barrier transistors*, Phys. Rev. Lett., 89 (2002), p. 106801.

[31] S. Sapmaz, C. Meyer, P. Beliczynski, P. Jarillo-Herrero, and L. Kouwenhoven, *Excited state spectroscopy in carbon nanotube double quantum dots*, Nano Lett., 6 (2006), pp. 1350–1355.

[32] M. R. Gräber, W. A. Coish, C. Hoffmann, M. Weiss, J. Furer, S. Oberholzer, D. Loss, and C. Schönenberger, *Molecular states in carbon nanotube double quantum dots*, Phys. Rev. B, 74 (2006), p. 075427.

[33] M. Gräber, M. Weiss, and C. Schönenberger, *Defining and controlling double quantum dots in single-walled carbon nanotubes*, Semicond. Sci. Technol., 21 (2006), pp. S64–S68.

[34] H. I. Jorgensen, K. Grove-Rasmussen, J. R. Hauptmann, and P. E. Lindelof, *Single wall carbon nanotube double quantum dot*, Appl. Phys. Lett., 89 (2006), p. 232113.

[35] J. U. Lee, P. P. Gipp, and C. M. Heller, *Carbon nanotube p-n junction diodes*, Appl. Phys. Lett., 85 (2004), pp. 145–147.

[36] J. Nygard and D. H. Cobden, *Quantum dots in suspended single-wall carbon nanotubes*, Appl. Phys. Lett., 79 (2001), pp. 4216–4218.

[37] L. I. Schiff, *Quantum Mechanics*, McGraw-Hill Education, 1968.

[38] D. J. Griffiths, *Introduction to Quantum Mechanics*, Prentice-Hall, NJ, 1994.

[39] M. Stopa, *Quantum dot self-consistent electronic structure and the coulomb blockade*, Phys. Rev. B, 54 (1996), pp. 13767–13783.

[40] G. Steele, *Imaging Transport Resonances in the Quantum Hall Effect*, PhD thesis, Massachusetts Institute of Technology, 2006.

[41] J. M. Thijssen, *Computational physics*, Cambridge University Press, New York, NY, USA, 1999.

[42] W. Kohn, *Nobel lecture: Electronic structure of matter-wave functions and density functionals*, Rev. Mod. Phys., 71 (1999), pp. 1253–1266.

[43] M. Fogler, *Ground-State Energy of the Electron Liquid in Ultrathin Wires*, Phys. Rev. Lett., 94 (2005), p. 56405.

[44] O. Wunnicke, *Gate capacitance of back-gated nanowire field-effect transistors*, Appl. Phys. Lett., 89 (2006).

[45] Z. Zhong, Y. Fang, W. Lu, and C. Lieber, *Coherent single charge transport in molecular-scale silicon nanowires.*, Nano Lett., 5 (2005), pp. 1143–6.

[46] C. van Rijmenam, *Spin filling in a few-hol silicon nanowire quantum dot*, master's thesis, TU Delft, 2007.

[47] J. H. Davies, *The Physics of low-dimensional Semiconductors*, Cambridge University press, 1998.

[48] E. Wigner, *On the interaction of electrons in metals*, Phys. Rev., 46 (1934), pp. 1002–1011.

[49] V. Deshpande and M. Bockrath, *The One-Dimensional Wigner Crystal in Carbon Nanotubes*, eprint arXiv: 0710.0683, (2007).

[50] M. Stopa, *Fluctuations in quantum dot charging energy and polarization*, Semicond. Sci. Technol., 13 (1998), pp. A55–A58.

[51] M. Stopa, *Rectifying behavior in coulomb blockades: Charging rectifiers*, Phys. Rev. Lett., 88 (2002), p. 146802.

[52] T. ANDO, *Spin-orbit, interaction carbon nanotubes : Condensed matter: Electronic properties, etc.*, J. Phys. Soc. Jpn., 69 (20000615), pp. 1757–1763.

[53] L. X. Benedict, S. G. Louie, and M. L. Cohen, *Static polarizabilities of single-wall carbon nanotubes*, Phys. Rev. B, 52 (1995), pp. 8541–8549.

[54] B. F., *Evidence of anisotropic metallic behaviour in the optical properties of carbon nanotubes*, Solid State Comm., 99 (August 1996), pp. 513–517(5).